

Geometry and mineral heterogeneity controls on precipitation in fractures: An X-ray micro-tomography and reactive transport modeling study

Catherine Noiriel, Nicolas Seigneur, Pierre Le Guern, Vincent Lagneau

▶ **To cite this version:**

Catherine Noiriel, Nicolas Seigneur, Pierre Le Guern, Vincent Lagneau. Geometry and mineral heterogeneity controls on precipitation in fractures: An X-ray micro-tomography and reactive transport modeling study. Advances in Water Resources, 2021, 152, pp.103916. 10.1016/j.advwatres.2021.103916 . hal-03218484

HAL Id: hal-03218484

https://minesparis-psl.hal.science/hal-03218484

Submitted on 9 May 2023

HAL is a multi-disciplinary open access archive for the deposit and dissemination of scientific research documents, whether they are published or not. The documents may come from teaching and research institutions in France or abroad, or from public or private research centers.

L'archive ouverte pluridisciplinaire **HAL**, est destinée au dépôt et à la diffusion de documents scientifiques de niveau recherche, publiés ou non, émanant des établissements d'enseignement et de recherche français ou étrangers, des laboratoires publics ou privés.



Distributed under a Creative Commons Attribution - NonCommercial 4.0 International License

Version of Record: https://www.sciencedirect.com/science/article/pii/S0309170821000713
Manuscript_33db404f6751e622896fac7a9dcb5ea0

Geometry and mineral heterogeneity controls on precipitation in fractures: an X-ray micro-tomography and reactive transport modeling study

Catherine Noiriel [1,*], Nicolas Seigneur [2], Pierre Le Guern [1], Vincent Lagneau [2]

[1] Géosciences Environnement Toulouse, UMR 5533 Université Paul Sabatier, CNRS, IRD, CNES, 31400 Toulouse, France

[2] MINES ParisTech, PSL University, Centre de Géosciences, 35 rue St Honoré, 77300 Fontainebleau, France

Catherine Noiriel* (corresponding author)

Pierre Le Guern

Géosciences Environnement Toulouse

UMR 5533 Université Paul Sabatier/CNRS/IRD/CNES

14, avenue Edouard Belin

31400 Toulouse, France

catherine.noiriel@univ-tlse3.fr (tel: +335 6133 4615)

Nicolas Seigneur

Vincent Lagneau

MINES Paris Tech

PSL University

Centre de géosciences

35, avenue Saint Honoré

77300 Fontainebleau, France

© 2021 published by Elsevier. This manuscript is made available under the CC BY NC user license
https://creativecommons.org/licenses/by-nc/4.0/

Abstract

The processes that affect reorganization of flow and transport in fractures during precipitation were investigated experimentally and numerically in order to highlight the interplay between calcite precipitation, flow and growth substrate. Calcite was precipitated from a supersaturated solution at two different flow rates (0.4 or 12 $cm^3 \cdot hr^{-1}$) into artificial fractures made in dolomitic limestone. Although the inlet fluid composition and temperature were identical for all the experiments, facture sealing and precipitation patterns were closely linked to the mineral substrate, fracture geometry and flow field reorganization. Calcite precipitation rate is highly variable along and between the flow paths and depends on the local saturation index of the reactive fluid. In addition, calcite precipitates preferentially on calcite comparatively to dolomite substrate. 2D reactive transport modelling accounting for the negative feedback between porosity and permeability decrease succeeded in quantitatively reproducing the experimental observations, such as the evolution of the fracture void obtained from X-ray micro-tomography (XMT), the evolution of the calcium breakthrough concentration and fracture sealing. The corresponding model was then used to evaluate the impacts of fluid flow and reactivity on randomly generated anisotropic fractures geometries. Simulation results reveal that the sealing capacity of fractures and associated reorganization of flow depends on the Damköhler number, i.e., the ratio between characteristic times for advective transport and reaction, although other factors like the fracture geometry and kinetic law play also a role at this stage. More importantly, the existence of a critical saturation index for initiating precipitation onto mineral substrate can substantially impair the prediction of the sealing capacity, and will depend on the spatial heterogeneity and connectivity of the mineral substrate. Most cases result in a strong precipitation gradient along the flow direction that will increase the permeability anisotropy. However, under certain conditions, precipitation allows the fracture to recover more isotropic properties that will lead back to a more uniform flow field and sealing. Negative feedback between precipitation process and transport during fracture closure supports a strong reorganization of flow of supersaturated fluids during geo-engineering operations.

Keywords

Calcite precipitation, reaction rate law, fracture sealing, dolomitic limestone, permeability, flow, X-ray microtomography, negative feedback, reactive transport modelling, critical saturation index.

Highlights

- Calcite precipitation depends on the substrate surface energy for nucleation
- Negative feedback between precipitation and transport promotes reorganization of the flow with time and sealing progress.
- Critical saturation index is an important parameter to account for during precipitation
- Sealing efficiency is dependent on the advective Damköhler, Da_{adv}
- Sealing efficiency also depends a lot on the shape of the reaction kinetic law and critical saturation index
- Mineral substrate heterogeneity strongly affects reorganization of flow during reactive transport

1. Introduction

Fractures are known to greatly influence the fate of fluids and contaminants in low permeability rocks. Reactive fluids have the potential to induce fractures [1-4], seal fractures [1, 5-9] or more generally, modify the fracture network [10, 11]. Their impact is significant on the preferential flowpaths through the host rock as well as on the global reactivity which, in turn, controls the fracture evolution [12, 13]. Understanding the reorganization of flow inherent to precipitation reactions within fractures is of interest for management of several geo-engineering applications. For applications such as CO_2 sequestration and mineral trapping [14-18] or biogrouting [19-21], carbonate rapid mineralization could take advantage of permeability reduction to increase storage safety. In contrast, a reduction of injectivity could challenge geothermal exploitation [10, 22]. However, in such shallow-depth and low temperature contexts, natural observations reveal that fractures are only partially filled with cement deposits, contrary to what is observed at greater depth and higher temperature [23]. At least, two hypotheses could explain this observation: (i) the sealing rate is too slow regarding the timescale and/or kinetics of mineral precipitation, in relation with the temperature, pressure and fluid composition, (ii) the deep reorganization of the flowpaths has diverted the reactive fluids away from the initial preferential precipitation paths, leading a large proportion of non-connected pores or compartmentalized areas to locally persist in the fracture void and reducing the self-sealing capacity. In any case, partial or complete sealing of opening-mode fractures results from complex and coupled physico-chemical processes.

Although the positive feedback between reactions, flow and transport has been largely studied for dissolution in porous media and fractures [5, 24-33], less studies have focused on the negative feedback that could develop during precipitation processes [19, 34-46]. However, with analogy to dissolution, the Péclet (Pe) and Damköhler numbers (Da), defined locally as: $Pe = v L^* / D_0$ and $Da = k_r L^{*2} / D_0$ (e.g., [29, 31]), where v is the fluid velocity ($m \cdot s^{-1}$), D_0 molecular diffusion ($m^2 \cdot s^{-1}$), k_r a first order kinetic constant (s^{-1}), and L^* a characteristic length (m), e.g. the fracture aperture, should be useful indicators to isolate different precipitation patterns and regimes. For instance, [47] mentioned that uniform precipitation of calcite can be obtained under rapid flow condition (high v) or only slightly supersaturated solution with respect to calcite (small k_r), thus isolating low Da and high Pe conditions for uniform precipitation. This observation is consistent with numerical results obtained by [36] using a model based on smoothed particle hydrodynamics. They distinguished between two compact regimes of precipitation, i.e., uniform compact at low Da and high Pe, and non-uniform compact at higher Da. A third, dendrite-like regime, might exists at very high Da [36, 48, 49]), although unlikely to be observable in natural conditions. When precipitation results from the injection of a supersaturated solution, the sole existence of compact regimes may result from the rapid depletion of reactants along the flow paths, thus leading to preferential precipitation near the inlet boundary. The non-linear dependency of the reaction rate to oversaturation should exacerbate this trend [50, 51]. Indeed, the highest the saturation index (log Ω), the strongest the dependence, with an exponent n of the kinetic law greater than one when growth occurs by the spiral mechanism at both edges and screw dislocations, or by 2D nucleation [52].

However, although Pe and Da can provide useful information about the evolution of a particular system, their use can be limited [53] or complex to handle with, especially when the reaction rate varies of several orders of magnitude along the flowpaths (i.e., between far-from-equilibrium and close-to-equilibrium conditions), when boundary conditions differ from flow of a supersaturated solution (e.g., when precipitation results from solute mixing [54], or when rock heterogeneities exert a first-degree influence on the local flow and transport conditions [8, 55-57]. The fact that their value evolves with reaction progress drives us to define reference numbers at the time of injection ($t = 0$) and fracture inlet ($x = 0$), namely Da_0 and Pe_0.

In addition, even under similar flow and chemistry conditions, crystal growth dynamics might be different from a uniform covering at the surface. Observations of dotted or more spread cement bridges in several fractures [6, 23, 58, 59] point toward a preferential nucleation and growth on some mineral substrate similarly to what has been observed in porous media [53, 60] giving to substrate surface energy an important role in initiating nucleation and growth [61-64]. The ability of the smallest pores to maintain

115 a higher saturation with respect to crystallization is another source of precipitation heterogeneity [65, 66].
116 Variation in growth rate of different crystal facets, development of crystallographic preferred orientations,
117 changes in specific surface area as competition for growth between neighboring crystals complicate the
118 geometry evolution through time [67-70]. Theses aspects are worth consideration, especially during
119 syntaxial or antitaxial growth in fractures.

120 The impact of precipitation on the morphology and microstructure of fractures is currently a limitation
121 in reactive transport modelling [23], most models relying on a continuum description at the representative
122 elementary volume (REV) scale, e.g., [71]. However, several approaches are emerging to account for the
123 impact of precipitate on fracture geometry evolution. For instance, investigation of precipitation using the
124 level set method [37, 72] or lattice Boltzmann methods [37, 57, 73, 74] are particularly interesting as they
125 permit to evaluate, in relationship with spatial mineral substrate heterogeneity, the effect of new
126 precipitate localization on the flow and transport properties. At the continuum scale, it is also possible to
127 account for the feedback between flow and reactions and between the volume of precipitate and
128 permeability, through implementation of porosity-permeability relationship [75-77]. While these laws
129 have allowed continuum-scale models to reproduce experimental results, e.g., [78, 79], their use near
130 clogging conditions have had limited success, as emphasized by relatively high discrepancies in modelling
131 results [80]. Micro-continuum models provide an alternative to continuum-scale models. These models
132 describing the evolving fracture aperture field allow for capturing the processes that are important to
133 fracture geometry alteration [81], and can lead to a better understanding of the relevant processes and
134 parameterization of continuum models.

135 In the present study, a combination of experiments, micro-scale characterization and micro-continuum
136 reactive transport modelling was performed to elucidate the relative contribution of chemical reactions and
137 transport to flow reorganization and fracture sealing. The objectives are to investigate how the flow rate,
138 the kinetic law, the fracture aperture distribution and mineral substrate heterogeneities at the fracture walls
139 affect precipitation as well as reorganization of flow and reactive transport through time. For this purpose,
140 we investigated experimentally precipitation in four artificial fractures of simplified geometries at two
141 different flow rates. Precipitation rates were calculated from effluent concentrations and 3D image
142 difference obtained using X-ray microtomography (XMT). Experimental results were then used to
143 constrain reactive transport modeling in more complex fracture geometries. Different simulation
144 configurations were tested to evaluate the impacts of three factors on the negative feedback between
145 chemistry, transport and permeability reduction in fractures: (i) reactive transport conditions, (ii) fracture
146 geometry and anisotropy, and (iii) mineral heterogeneity distribution at the fracture walls.

2. Materials and methods

2.1. Flow-through laboratory experiments in fractures

Four flow-through experiments were carried in artificial fractures made in a dolomitic limestone of Tithonian age (Upper Jurassic) sampled in a quarry (Crayssac, Lot, France). The rock composition given by X-ray diffraction (XRD) analysis is about 50% calcite and 50% dolomite, with a minor amount of quartz and K-feldspar. The carbonate matrix is composed of a microsparitic cement of calcite and dolomite.

Table 1 summarizes the experimental conditions. A block was sewed, drilled and possibly grooved to provide four cylindrical samples of 50±1 mm in length and 25 mm in diameter with three different fracture geometries, i.e., planar (sample CRA1FA), planar with two channels of 2.0 ± 0.3 mm in width and 500 or 700 µm in depth grooved in the fracture plane (samples CRA2FA and CRA3FA), or trapezoidal (sample CRA4FA). The two fracture walls were glued together with epoxy resin after intercalating glass wedges on their edges to prevent for closure or opening of the fracture during experiment, resulting in a fracture width of 15 ± 1 mm. The external surface of the samples apart from the fracture inlet was also covered with epoxy resin to avoid precipitation. The surface of the fracture walls was estimated from their geometry with the addition of the inlet surface of the sample which was not covered with epoxy resin.

The inlet fluid used in the experiments was a 50-50% mixture of $CaCl_2$ and $NaHCO_3$ solutions prepared from reagent-grade salts dissolved in deionized water and equilibrated with atmospheric P_{CO2}. The composition of the mixture is 1.87 ± 0.03 mM $CaCl_2$ and 3.95 ± 0.07 mM $NaHCO_3$ and corresponds to a calcite saturation index (log Ω) of 1.38 (and so, a saturation state, Ω, of 24). After saturation and flushing with deionized water clean the fracture walls, the samples were injected at the flow rate Q_0 of either 0.4 $cm^3 \cdot h^{-1}$ using a syringe pump (samples CRA1FA and CRA2FA) or 12 $cm^3 \cdot h^{-1}$ using a peristaltic pump (samples CRA3FA and CRA4FA).

Table 1. Summary of the experimental conditions. *Experiment was stopped after sealing of the fracture inlet. **The minimum (a_{min}) and maximum (a_{max}) values of aperture of the trapezoid are deduced from XMT measurements at t_1 in the glued parts across the fracture width.

	CRA1FA	CRA2FA	CRA3FA	CRA4FA
Geometry	Planar	Planar with two	Planar with two	Trapezoidal

		grooved channels	grooved channels	
Initial aperture (µm)	a_{planar} 300	a_{planar} 170	a_{planar} 170	a_{min} 170, a_{max} 400**
Grooved channel depth (µm)	-	500 and 700	500 and 700	-
Geometric surface area of fracture walls (cm^2)	15.5	~16.0	~16.0	15.5
Q_0 ($cm^3 \cdot h^{-1}$)	0.4	0.4	12	12
Duration Δt (d)	40	40	16.7*	24.6*

175

176 ## 2.2. Quantitative determination of the extent of the reaction

177 ### 2.2.1. Determination of the global precipitation rate

178 Dissolution of dolomite being considered as negligible during the experiments, the amount of calcite
179 precipitated in the fractures was determined from chemical analyses throughout the experiments of the
180 difference in calcium concentration, ΔCa ($mol \cdot m^{-3}$), between the fracture inlet ($[Ca]_{in}$) and outlet ($[Ca]_{out}$).
181 The volume of precipitated calcite at time t_i is given by:

182 $$V_{cal}(t_i) = Q_0 \times \upsilon_{cal} \int_{t=t_0}^{t=t_i} \Delta \mathrm{Ca}(t)\, dt \qquad \text{Eq. 1}$$

183 with Q_0 the volumetric flow rate ($m^3 \cdot s^{-1}$) and υ_{cal} the molar volume of calcite ($m^3 \cdot mol^{-1}$). The global rate
184 of precipitation, R_{cal}, is given by:

185 $$R_{cal} = \frac{\Delta n}{\Delta t} = \frac{\Delta V_{cal}}{\upsilon_{cal}} \times \frac{1}{\Delta t} \qquad \text{Eq. 2}$$

186 with Δn the total amount of calcite precipitated (mol), and Δt the duration of the experiment ($\Delta t = t_1 - t_0$).

187 ### 2.2.2. Determination of the local precipitation rate and crystal growth rate

188 Local rates of precipitation within the fractures were evaluated from X-ray micro-tomography imaging
189 (XMT) and secondary electron microscopy (SEM) analysis of the crystals formed at the fracture wall

surfaces. Fracture geometries were characterized by X-ray micro-tomography on Phoenix Nanotom systems (Fédération de Recherche Fermat, FR 3089, Toulouse and UMR 7359 GéoRessources, Nancy), with a pixel size of 12.23 µm. The data sets were collected before (t_0) and after the experiments (t_1), except for CRA4FA whose geometry, assumed to be a perfect trapezoid, was not imaged at t_0 and was deduced from measurements near the fracture wedges at t_1. As precipitation was localized near the sample inlet, only the upper part close to the inlet was imaged at t_1. Image processing was carried out using Avizo® software. Once the data sets were segmented, an algorithm was used to extract the fracture walls and aperture (see [82] for the procedure of fracture wall and aperture extraction). The data sets were also registered to permit localization of precipitation within the fracture from volume subtractions, i.e., $V(t_1) - V(t_0)$, with $V(t_0)$ and $V(t_1)$ the 3D fracture volumes at t_0 and t_1, respectively. Image difference can lead to the determination of the local rate of precipitation, r_{cal}, (mol·s^{-1}), assuming that the reactive surface area S_r and geometric surface area S_{pix} (m^2) are equal:

$$r_{cal} = \frac{\Delta n_{x,y}}{\Delta t} = \frac{\Delta a_{x,y}}{\Delta t} \times \frac{1}{v_{cal}} \times S_{pix} \qquad \text{Eq. 3}$$

with $\Delta n_{x,y}$ the local amount of calcite precipitated (mol), and $a_{x,y}$ the local fracture aperture (m).

Given the resolution of the imagery, the limit for difference in aperture detection is about two pixels, i.e. ~25 µm. After the flow-through experiments, the fractures were opened to examine the new crystal location and morphology. SEM stood in for XMT to characterize the geometry of the new crystals with a finer resolution. Average crystal size was evaluated at different locations of the fracture walls from size measurement on about 30 crystals each time.

2.3. Reactive transport modelling

2.3.1. Description of the model

The 2D multi-component reactive transport model HYTEC [83, 84] was used to simulate fracture geometry evolution as a result of calcite precipitation. HYTEC is based on the operator-splitting approach, solving the flow and advection-dispersion-reaction problems sequentially. In particular, the model accounts for the feedback between calcite precipitation and the resulting changes of fracture porosity, permeability and flow.

In the model, the fractures are discretized in a 2D mesh that approximates the geometry of the fracture planes. In each grid cell, the porosity is related to the local fracture aperture, $a_{x,y}$, by:

$$\phi_{x,y} = \frac{a_{x,y}}{d_z} \quad \text{Eq. 4}$$

where d_z is the thickness of the domain perpendicular to the fracture wall (10^{-3} m), and permeability is computed using the relationship derived from the Hagen-Poiseuille solution of the Navier-Stokes equations, e.g., [85]:

$$k_{x,y} = \frac{a_{x,y}{}^2}{12} \quad \text{Eq. 5}$$

The saturated flow is described by:

$$S_s \frac{\partial h}{\partial t} = \vec{\nabla} \cdot (K \vec{\nabla} h) \quad \text{Eq. 6}$$

where S_s is the specific storage coefficient (m^{-1}), K is the hydraulic conductivity ($m \cdot s^{-1}$) and h is the hydraulic head (m). Hydraulic conductivity and permeability are related through the following expression:

$$K = \frac{\rho g}{\mu} k \quad \text{Eq. 7}$$

where g, ρ and μ represent the gravitational acceleration (9.81 $m \cdot s^{-2}$), fluid density (1000 $kg \cdot m^{-3}$) and viscosity (10^{-3} Pa·s), respectively, all assumed constant in these simulations.

The boundary conditions to the flow problem represent a constant injection rate at the top inlet of the domain along the x-direction, and a constant pressure ($h = 0$) at the bottom outlet, while the left and right boundaries are impermeable. The flow equation is solved to provide the hydraulic head h (m) in each grid cell. The fluid velocity is then computed based on Darcy's law [86]:

$$\mathbf{v} = -K \vec{\nabla} h \quad \text{Eq. 8}$$

The computed fluid velocity is then used to solve the reactive transport problem:

$$\frac{\partial(\phi \Psi_i)}{\partial t} = \nabla \cdot (\phi \mathbf{D} \nabla \Psi_i - \mathbf{v} \Psi_i) - \phi \sum_m \nu_{i,m} R_m \quad \text{Eq. 9}$$

where Ψ_i is the total concentration of component i ($mol \cdot l^{-1}$), $\mathbf{D}$ is the dispersion tensor ($m^2 \cdot s^{-1}$), R_m is the kinetically-controlled mineral reaction term ($mol \cdot l^{-1} \cdot s^{-1}$), m is the number of minerals, and $\nu_{i,m}$ is the stoichiometric coefficient for the reaction.

The reaction rate of minerals is described by [87], and we used the kinetic rate constant $k_{cal} = 1.79\ 10^{-9}$ mol·m^{-2}·s^{-1} and the exponent n = 1.12 obtained from continuously-stirred precipitation experiments on calcite seeds [51]. The overall calcite precipitation rate, R_{cal} (mol·l^{-1}·s^{-1}), is defined differently depending on whether it occurs on the calcite or dolomite substrate, by introducing a critical saturation state, $\Omega_{crit,dol}$, to initiate nucleation onto dolomite substrate:

$$R_{cal} = k_{cal} \times \left(S_{cal} + \delta\left(\frac{\Omega_{cal}}{\Omega_{crit,dol}}\right) S_{dol} \right) \times (\Omega_{cal} - 1)^n \qquad \text{with } \delta(a) = \begin{cases} 1 \text{ if } a > 1 \\ 0 \text{ otherwise} \end{cases} \qquad \text{Eq. 10}$$

where S_{cal} and S_{dol} (m^2·l^{-1}) are the specific surface area of calcite and dolomite, respectively, a is the ratio $\Omega_{cal} / \Omega_{crit,dol}$, and Ω_{cal} is the saturation state with respect to calcite ($\Omega_{cal} = \text{IAP} / K_{sp}$, with K_{sp} the solubility product and IAP the ion activity product). Precipitation of calcite starts onto dolomite substrate when $\Omega_{cal} > \Omega_{crit,dol}$, whereupon the critical saturation state returns to 1.

As mineral growth is expected to increase the specific surface area of mineral *m* [51, 54], we choose to express it as:

$$S_m = S_0 + S_{growth} \qquad \text{Eq. 11}$$

where S_0 is the initial specific surface area, and S_{growth} is dependent on the volume fraction of solid precipitated. Unless explicitly mentioned, S_{growth} was taken equal to 0.21 m^2·g^{-1} (value obtained by [51] for calcite seed crystals after precipitation experiments). As a result, the precipitation rate will increase during precipitation, thus explaining a regular decrease in $[Ca]_{out}$ with time. In contrast, S_{growth} = 0 m^2·g^{-1} would maintain a quasi steady-state $[Ca]_{out}$, the variation of which would only result of changes in the fluid resident time in the fracture void, in relationship with the changes in the flow field during sealing.

The diffusion coefficient, D_0, is equal to 7.9 10^{-10} m^2·s^{-1} and corresponds to the diffusion coefficient of Ca^{2+} at 25°C [88]. The dispersion tensor **D** is reduced to two dispersion-diffusion coefficients, i.e., $D_x = D' + 0.5\Delta x + D_0$ longitudinally, and $D_y = D' + D_0$ transversally, where D' is the dispersion coefficient, set arbitrarily to 0.1 mm based on the fracture dimensions, and $0.5\Delta x$ represents the numerical dispersion, i.e., half of the mesh length. This way, the longitudinal dispersivity remains about 3 times higher than the transverse dispersivity. Transport (Eq. 9) is solved using the sequential iterative approach, during which the evolution of the fracture aperture (or porosity) is computed based on the evolution of the

mineral volume fraction. The feedback on flow is treated explicitly after updating the local permeability following the Kozeny-Carman relationship [89]:

$$k_{x,y} = k_{0\,x,y}\left(\frac{\phi_{x,y}}{\phi_{0\,x,y}}\right)^3\left(\frac{1-\phi_{0\,x,y}}{1-\phi_{x,y}}\right)^2 \qquad \text{Eq. 12}$$

where $k_{0\,x,y}$ and $\phi_{0\,x,y}$ are the initial local permeability and porosity, respectively. The volume fractions of calcite precipitated in the pore space can be evaluated from the porosity change:

$$V_{f-cal} = 1-\left(\phi_{x,y}/\phi_{0\,x,y}\right) \qquad \text{Eq. 13}$$

or equivalently from the amount of calcite precipitated in the solid phase ($m^3 \cdot m^{-3}$):

$$V'_{f-cal} = V_{cal}/V_{rock} = [\text{Calcite}]\,\phi_{x,y}\nu_{cal} \qquad \text{Eq. 14}$$

where V_{rock} is the volume of rock in the mesh, and [Calcite] is the corresponding concentration of calcite ($mol \cdot l^{-1}$).

Throughout the simulations, the porosity and permeability fields are extracted to compute the effective permeability at the fracture scale, in directions parallel ($\langle k_x \rangle$) and perpendicular ($\langle k_y \rangle$) to the main flow direction. Indeed, while local permeability is isotropic and evolves following the Kozeny-Carman relationship, the effective permeability at the fracture scale can display different properties, due to non-uniform evolution of the local permeability field. To evaluate the evolution of effective permeability of the considered media, flow (Eq. 6) is solved using a head-imposed configuration between two parallel boundaries, similarly to permeameter conditions [90]. The homogenized values of the hydraulic conductivity in the *x*- and *y*-direction are thus computed based on stationary fluid flow.

2.3.2. Simulation setup

Several sets of simulations using nine different fracture geometries were set up to better understand the different processes involved during precipitation in fractures. In particular, we explore the influence of: (i) reactive transport parameters (i.e., fluid reactivity and injection rate, thanks to the advective Damköhler, Da_{adv} [77]), (ii) fracture geometry, and (iii) mineral heterogeneity distribution at the fracture walls, on the flow path evolution and permeability reduction in fractured media. Testing different configurations is motivated by the experimental observations, where these parameters have shown to play a role in the fracture filling and flow reorganization.

First, reactive transport modelling of the experiments was performed to validate and calibrate the model. The three first fracture geometries used in the simulations are the planar fracture, the planar fracture with two grooved channels and the trapezoidal fracture, whose geometry is derived from the XMT imaging. The fracture void domains of 50.0×15.0 mm are meshed with a 100×30 grid size (Figure 1). The initial and boundary conditions for fluid chemistry and flow are similar to the experiments (Table 1). The injected flow rate is imposed at the sample inlet in the *x*-direction, while a constant atmospheric pressure is set at the outlet. The other external boundaries are no-flow boundaries. Calcite and dolomite substrates are set in first instance as a continuum in every mesh in a 50/50 proportion, with an equal initial specific surface area ($S_{cal} = S_{dol}$). In a first approach, precipitation is assumed to occur equally on both calcite and dolomite. Secondly, a critical saturation state $\Omega_{crit,dol} = 10$ for precipitation onto dolomite is set. This value was selected based on the SEM observations of calcite growth onto dolomite matched against the saturation state maps obtained in the first set of simulations (see further in section 3.1). The specific surface area is adjusted to fit with the calcium concentration measured at the sample outlet for experiment CRA3FA.

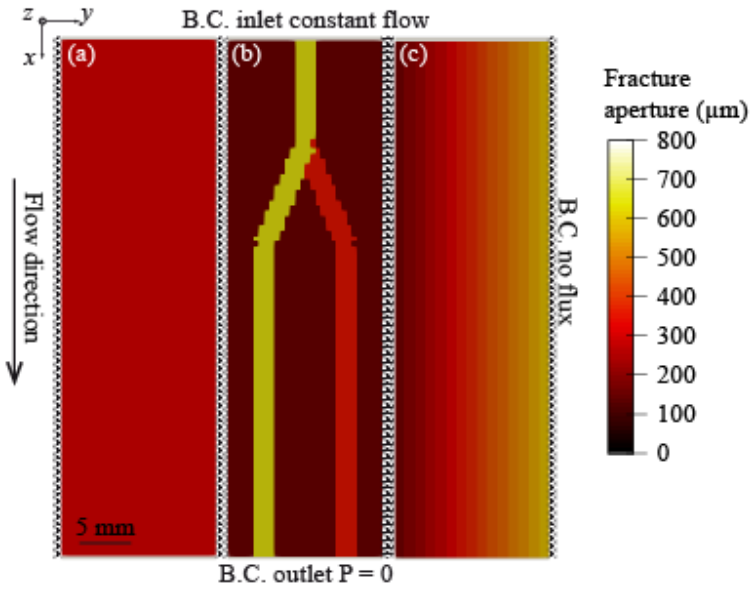


Figure 1. Fractures geometries used in the simulations, (a) planar, (b) planar with two grooved channels and (c) trapezoidal. The simulation setup and boundary conditions (B.C.) are also shown.

In addition to modelling of the experiments, six model fractures (Figure 2a) with a geometry more representative of natural fractures whose walls would experience an increase degree of shearing were generated using the SynFrac® software [91]. The motivation for simulating reactive transport in synthetic

fractures is threefold. First, the geometries used in the present experiments are simplistic and the results are not meant to be extrapolated to natural media. Second, the fluids commonly used to run experiments in the laboratory [43, 44, 51, 92, 93] or in the field [19] are far oversaturated compared to saturation state encountered in most of natural waters, the log of which rarely exceeds 1, so that the reactivity relevant to natural settings should be lower. The choice of a high saturation index in experiments is linked to the precipitation rate of calcite, which decreases exponentially along the fracture (Eq. 10), thus constraining the duration of the experiments, the latter being shorter (a few days/weeks) when supersaturation is exaggerated. The counterpart of this is a sharp reaction front [44, 50, 51, 70, 93] driving to a rapid sealing of the sample inlet during experiments, where precipitation rate is orders of magnitude higher than a few mm/cm further. However, calibrating the model using well-constrained experiments should permit extension of its application to more natural conditions (i.e., with lower R_{cal}). Third, generating fracture allows for controlling the degree of geometric anisotropy of the fracture aperture parallel or perpendicular to the flow direction, and for evaluating the effects of fracture wall mismatch and of the mineral heterogeneity distribution on the capacity of fractures to self-healing.

The six different fracture geometries are set up from three starting fracture aperture fields generated with SynFrac®, which differ by their anisotropy factor (AF = 1, 2, and 4). The grid size is 64×64, and the geometry of the fracture walls is periodic. The aperture distributions are close to Gaussian distributions, with a mean aperture a_m of 400 ± 1 µm and a standard deviation σ_a of 152 ± 2 µm, leading to a roughness factor σ_a / a_m of ~0.38; these values are consistent with data measured in natural limestone fractures after dissolution process [82, 94]. From these aperture fields, six different fracture geometries of 128×64 grid sizes (51.2×25.6 mm) are derived. In the first cases, the initial aperture fields are duplicated in the *x*-direction to generate fracture geometries, whose direction of stretching of the aperture field is parallel (//) to the flow direction, resulting in a higher correlation length λ_x in the *x*-direction. In the second cases, the initial aperture fields are first rotated 90°, and then duplicated in the *x*-direction to generate fracture geometries whose aperture field direction of stretching is perpendicular (⊥) to the flow direction, resulting in a higher correlation length λ_y in the *y*-direction.

Table 2 summarizes the three sets of simulations with their investigated parameters. The first set of simulations focuses on the impact of reactive transport on the evolution of the precipitate distribution in the fracture void and the reorganization of flow, and thus the fracture anisotropy and the mineral heterogeneity distribution are kept invariant. For that, we define the advective Damköhler number at time *t* = 0, which is to some extent equivalent to Da_0 / Pe_0, as:

$$Da_{adv,0} \propto \alpha \frac{R_0}{v_0} \equiv \alpha' \frac{R_0}{Q_0} \qquad \text{Eq. 14}$$

where R_0 and v_0 are the rate of calcite precipitation ($R_{cal,0}$) and the fluid velocity at t_0, respectively, and α and α' are coefficients.

The initial geometry used in that set of simulations is {AF = 1; //}. Calcite nucleation is first assumed to occur homogeneously and at the same rate at the fracture walls, so that calcite and dolomite are set in a 50/50 proportion in every mesh, with an equal specific surface area ($S_{cal} = S_{dol}$). Both the injection rate and the mineral reactivity are increased or decreased compared to the experimental conditions to investigate a range of $Da_{adv,0}$ spanning five orders of magnitude. A reference injection rate ($Q_{0-ref} = 12\ cm^3 \cdot h^{-1}$) and precipitation rate at the fracture inlet ($R_{0-ref} = 1.44\ 10^{-7}\ mol \cdot l^{-1} \cdot s^{-1}$, with n = 1.12, Eq. 10) are set from the modelling conditions in fracture CRA3FA in order to define at the inlet the reference $Da_{adv,0-ref} = \beta$. Eight values of $Da_{adv,0}$ ranging from 0.1 to 300 β are explored by varying the injection rate ($Q_{0-ref}/300 \le Q \le Q_{0-ref}$) and/or the precipitation rate ($R_{0-ref}/100 \le R_{cal,0} \le R_{0-ref}$) to mimic injection of less reactive fluids at slower velocities. The quantity $R_{cal,0} / R_{0-ref}$ is defined as the reactivity factor (RF) in the simulations (Table 2). Evaluation of the dependence of the precipitation rate to the order of reaction was also achieved in a simulation using a lower exponent n = 0.65 in the kinetic formulation (Eq.10); k_{cal} was increased about 4 times to keep the same R_{0-ref} and reactivity factor RF =1 than in the reference simulation.

Simulations are stopped either when complete sealing of the fracture is achieved, i.e., for a permeability in the flow direction $\langle k_x \rangle << 10^{-11}\ m^2$), or when porosity reduction has reached a sufficient low value (~10-15%) regarding the duration of the simulation.

The second set of simulation evaluates the impact of the fracture anisotropy in relationship to the flow direction, i.e., parallel or perpendicular to the aperture stretching direction. In these simulations, the six fracture geometries {AF = 1,2,4; ⊥,//} are used. Precipitation is still assumed to occur homogeneously on both calcite and dolomite at the fracture walls. The same values of $Da_{adv,0}$ than in the first set of simulations are explored.

The third set of simulations accounts for the variability in mineral distribution at the fracture walls and for the existence of a critical saturation state $\Omega_{crit,dol}$ to initiate precipitation onto dolomite substrate. In these simulations, the mineral distributions are mapped on the fracture geometry {AF = 4; //} with

372 $Da_{adv,0} = \beta$, and the simulations are compared with the previous simulation assuming a 50/50 mineral
373 proportion in every mesh (continuum representation of the mineral substrate). Three values of $\Omega_{crit,dol}$ are
374 tested, i.e., 10, 20 and 30. The first value is derived from the experimental observations (see further in
375 section 3.1). The second further restricts precipitation onto dolomite. In the last case, precipitation onto
376 dolomite is impossible, due to the fact that $\Omega_{crit,dol} > \Omega_{cal,0}$. This case mimics what could happen when the
377 critical saturation state with respect to a mineral is never reached, and how it would affect fracture sealing.
378 Six types of spatial distribution of minerals including three different mask patterns are considered. Mineral
379 spatial heterogeneity is considered by varying the spatial distribution of calcite and dolomite volume
380 fraction in every mesh, with 50% of the meshes considered to contain only calcite and 50% only dolomite.
381 In the four first cases, classification of the meshes is based from the generation of a 128×64 random field
382 with uniform standard distribution. To create the first random distribution, the 50% smallest values are set
383 to calcite (Mask 1), defining small mm-size clusters as isolated spots of mineral of 400×400 μm^2. In this
384 case, the mineral phases, i.e. calcite or dolomite clusters, are not connected through the fracture. In the
385 second random distribution (Mask 2 and inv-Mask2), the 1.5% smallest values are picked up as small
386 calcite or dolomite spots and clusters are grown until the mineral fraction has reached 50% of the domain.
387 For these cases, isolated spots of about 3×3 mm^2 and cm-size clusters are defined and only one mineral
388 phase is connected through the fracture. In the last two cases, calcite and dolomite are correlated to the
389 local aperture distribution. In this case, both mineral phases are connected through the fracture. The 50%
390 largest local apertures are either assigned calcite (Mask 3) or dolomite (inv-Mask 3). Mask3 configuration
391 aims to evaluate the influence of pre-existing fracture alteration prior to precipitation in multi-mineral
392 rocks. The case calcite is assigned the largest apertures mimics a small degree of alteration of the fracture
393 prior to precipitation, where the higher dissolution rate for calcite compared to dolomite [95] would
394 increase the fracture aperture in areas calcite is present [96, 97]. The case dolomite is assigned the largest
395 apertures is the complementary case. The different masks are presented in Figure 2b.
396

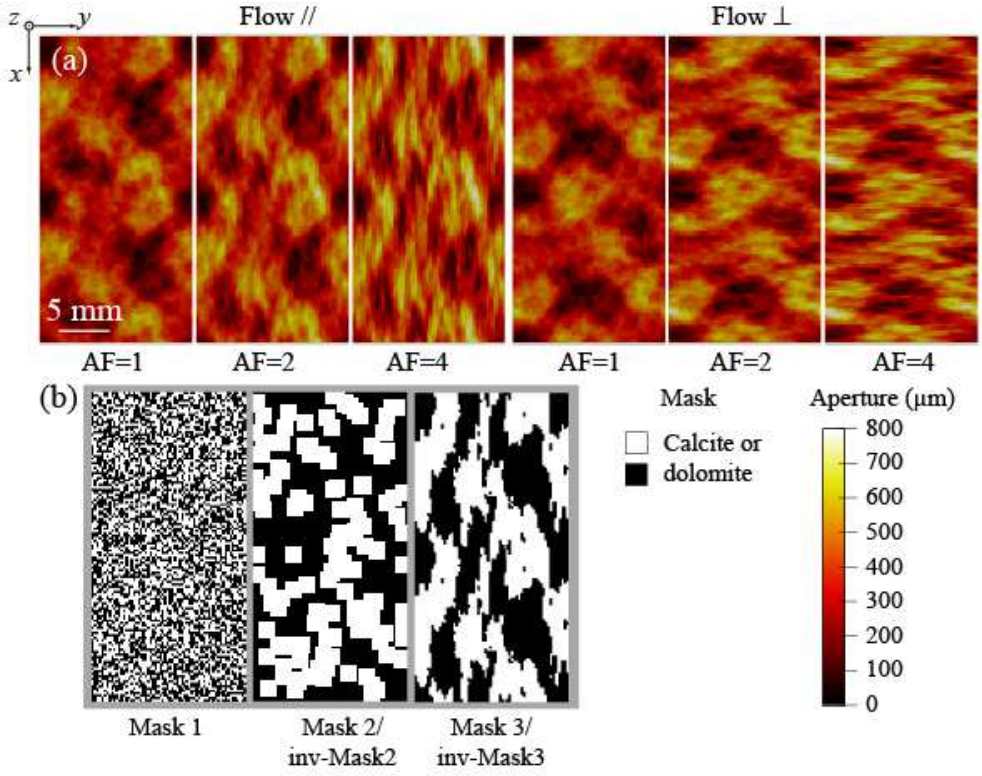


Figure 2 (a) Fractures geometries used in the simulations with their nomenclature {AF = 1,2,4; ⊥,//}, and (b) masks used to set mineral heterogeneity distribution in the fracture domain. The white and black colors represent either calcite and dolomite (Masks 1 to 3), or dolomite and calcite (inv-Masks 2 and 3), respectively.

Table 2. Summary of the modelling cases in the synthetic fractures.

Parameters explored	Reactive transport conditions			Fracture and flow anisotropy		Fracture wall mineral substrate	
	Reactivity factor and exponent {RF,n}	Flow rate Q_0 ($cm^3 \cdot h^{-1}$)	$Da_{adv,0}$	Anisotropy factor AF	Stretching direction	Mineral heterogeneity	$\Omega_{crit,dol}$
1st set	{1,1.12} (R_{0-ref}),	0.04, 0.4 and 12	0.1, 0.3, 1, 3, 30,	1	// to the flow direction	50-50 calcite dolomite in a continuum	no

	{0.1,1.12}, {0.01,1.12}, and {1,0.65}	(Q_{0-ref})	300 β				
2nd set	{1,1.12}, {0.1,1.12}, and {0.01,1.12}	0.04, 0.4 and 12	0.1, 0.3, 1, 3, 30, 300 β	1,2,4	// or $\perp$ to the flow direction	50-50 calcite dolomite in a continuum	no
3rd set	{1,1.12}	12	β	4	// to the flow direction	50-50 calcite dolomite in a continuum, small (Mask 1), and large (Mask 2 and inv-Mask2) randomly generated clusters, aperture-correlated clusters (Mask 3 and inv-Mask3)	10, 20, and 30

3. Experimental results

3.1. Calcite nucleation and growth at the fracture walls

The size, orientation, and density of the calcite crystals newly precipitated at the fracture wall surfaces is highly variable and closely related to the calcite precipitation rate, which depends on the mineral

409 substrate, the local saturation state with respect to calcite, Ω_{cal}, and the local flux of reactants along the
410 flowpaths.

411 XMT image difference between t_1 and t_0 and SEM imaging after the experiments allow for
412 determination of the areas where precipitation occurred. In all samples, precipitate amount is higher near
413 the inlet of the fractures, where Ω_{cal} is the highest, and the crystal size and density are shown to decrease
414 progressively from the inlet to the outlet (Figure 3). Growth of calcite proceeds by growth of heteronuclei
415 on mineral substrate. Polycrystal growth results in blocky microstructures with epitaxial growth on
416 existing micro-sparite seed crystals. The crystals are randomly oriented due to the multitude of
417 orientations depicted by the seed crystals in the rock. It is worth noting that a few dumbbell aragonite
418 crystals are also noticed in the fracture void.

419 At low flow rate (CRA1FA and CRA2FA), the fracture aperture reduction is scarce and cannot be
420 caught properly with XMT. However, individual crystals and crystal clusters are noticed at the fracture
421 walls (Figure 3a). At high flow rate (CRA3FA and CRA4FA), equant crystals grew on most of the
422 fracture wall surfaces near the inlet, whereas further in the fractures, crystals grew preferentially onto
423 calcite substrate compared to dolomite substrate (Figure 3b). This effect has an increasing impact as far as
424 the average crystal size decreases, i.e., toward the outlet, suggesting that nucleation on dolomite substrate
425 requires a higher energy and so a higher critical saturation index (log $\Omega_{crit,dol}$). Crossing of SEM
426 observations of precipitate onto dolomite with modelling of experiment CRA3FA (see section 4.1) gives
427 an estimate of $\Omega_{crit,dol}$ of 10. It is worth noting that precipitation is unlikely to initiate at the surface of
428 silicates (i.e., quartz and K-feldspar, Figure 3, inserts 5 and 6), which remains uncovered until crystals
429 grown on carbonates are big enough to combine (Figure 3, insert 4).

430 Precipitation is also localized in the areas of preferential flow (Figure 3b), where crystals can be a
431 dozen times bigger than in the areas of lower aperture. Multiple crystal orientations involving different
432 facet growth rates and competition between neighboring crystals [67] that result in enclosed crystals are
433 also visible locally (despite Ω_{cal} is assumed to be identical) and contribute to the growth rate
434 heterogeneity (Figure 3, insert 4). Different induction times for precipitation [60, 98] and Ostwald
435 ripening [99, 100] are other causes that can explain the difference in crystal sizes.

436 Fracture sealing was observed at the inlet of samples CRA3FA and CRA4FA at high flow rates, after
437 16.7 and 24.6 days of experiment, respectively. Sealing was indicated by an expulsion of the sample from
438 the jacket due to an abnormal pressure increase at the inlet, which indicates that permeability was reduced
439 to a value below 10^{-11} m^2 (assuming a pressure of 0.2 MPa at the inlet), thus corresponding to a hydraulic

aperture of about 10 µm. Although it corresponds more to partial sealing rather than complete sealing –for which fracture permeabilities are reported in the range 10^{-14}-10^{-17} m^2 [10, 101]–, we can infer that complete sealing is close.

For CRA3FA, sealing corresponds to the closure of both the 170 µm-width planar fracture surface and the 700 µm-deep main channel inlet. For CRA4FA, sealing corresponds to the closure of the trapezoidal inlet of minimum and maximum apertures of 170 µm and 400 µm, respectively. However, it is worth noting that the main channels close to the inlet remain micro-porous despite fracture sealing.

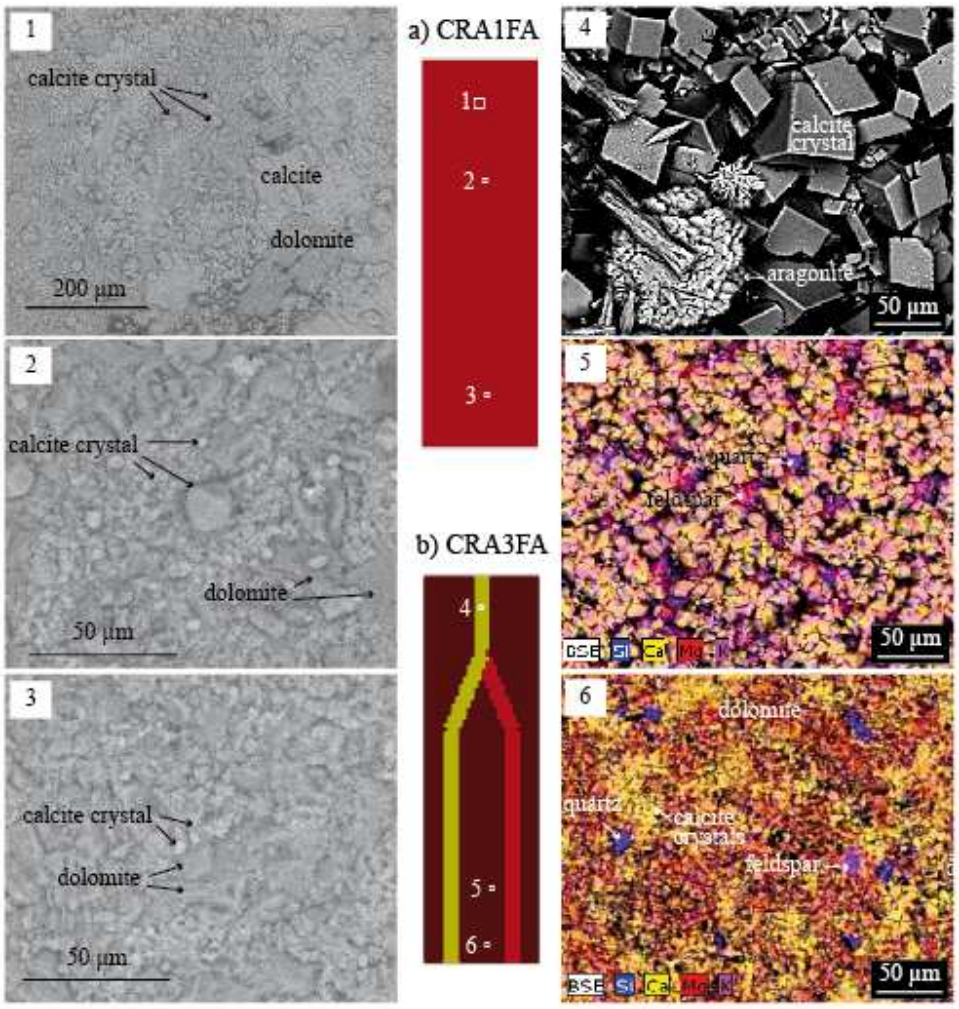


Figure 3. SEM observations of calcite precipitate on fracture walls for samples (a) CRA1FA and (b) CRA3FA. The location of the observation zones is indicated on the simplified geometry of the samples. (a) A decrease in the crystal size along the flow direction is observed, as well as preferential nucleation and growth of crystals onto calcite compared to dolomite substrate; (b) Decrease in calcite amount

overlaying on the dolomite mineral substrate along the flow direction. Note also that precipitation is unlikely to happen on the silicates. Calcite is highlighted on the SEM-EDX (Energy Dispersive X-Ray analysis) images by Ca (yellow), dolomite by Mg (red), silicates by Si (blue) and K (pink).

3.2. Fracture sealing rate

3.2.1. Quantitative determination of the extend of the reaction

The volume of calcite precipitated and the fracture-scale sealing rate were estimated from ΔCa between the sample inlet and outlet (Table 3). The amount of precipitate is over one order of magnitude higher for samples at high flow rate compare to low flow rate. However, the average $[\overline{Ca}]_{out}$ is quite similar for all the experiments, indicating that kinetics globally controls the precipitation rate over the flow rate or the fluid resident time. At high flow rate, however, a 30-time shorter resident time in the experiments explains why the global precipitation rate is 20 to 36 times higher compared to low flow rate.

Table 3. Quantitative extend of the reaction determined from chemical analyses.

	CRA1FA	CRA2FA	CRA3FA	CRA4FA
Average $[\overline{Ca}]_{out}$ ($\times 10^{-3}$ mol·l^{-1})	1.65	1.51	1.64	1.61
Volume precipitated (mm^3)	3.1	5.0	41.1	68.4
Global precipitation rate R_{cal} (mol·s^{-1})	2.4 10^{-11}	4.0 10^{-11}	7.7 10^{-10}	8.7 10^{-10}

3.2.2. Local precipitation rate based on imagery

Following Eq. 3, the local precipitation rate can also be calculated and mapped for samples CRA3FA and CRA4FA, as shown in Figure 4. The precipitation rate is higher close to the fracture inlet, where supersaturation was the highest, and decreases very quickly along the samples. The precipitation rate is also higher in the channels. For CRA3FA, the fracture closure rate near the inlet is about 8 µm·d^{-1} in the main channel (up to 25 µm·d^{-1} for some single crystals) and 5 µm·d^{-1} in the planar sides. The local rates in the two diverted channels are somewhat equivalent, although both XMT and SEM observations show that they are higher in the deeper channel. Two plumes with a high precipitation rate are also observed at each inlet termination, i.e. next to the impermeable boundaries, and certainly underline the final injection paths

that preceded sealing. For CRA4FA, the fracture closure rate near the inlet and in the area of higher aperture is about 5 µm·d^{-1} in, whereas it is only 3 µm·d^{-1} in the area of lower aperture.

For CRA1FA and CRA2FA at low flow rate, X-ray micro-tomography was not enough resolved to quantify changes in the fracture geometry. However, analysis of crystals using SEM show the same patterns than for CRA3FA and CRA4FA, although the crystal size is smaller, e.g. from 15.8±7.3 µm to 0.5±0.2 µm between the inlet and outlet for CRA1FA. Assuming roughly that the crystal size is equivalent to the aperture reduction, this results in a fracture closure rate of about 0.4 µm·d^{-1} near the inlet, which reduces to about 0.01 µm·d^{-1} near the outlet.

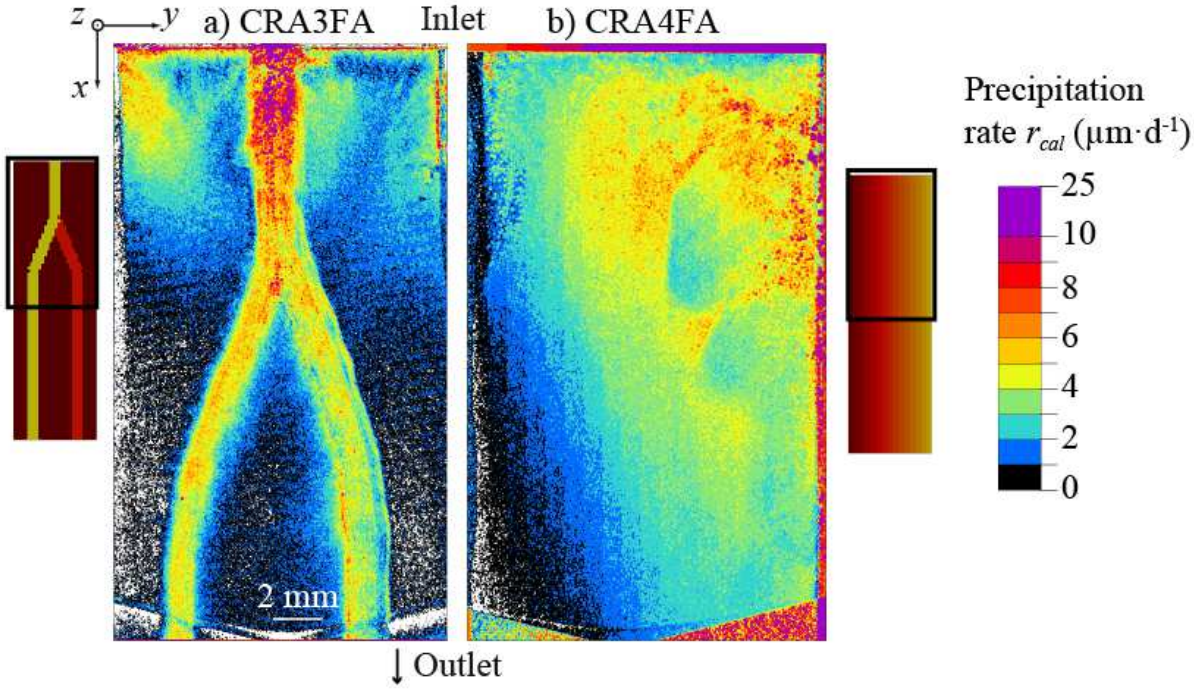


Figure 4. Precipitation rate map calculated from XMT data sets for samples (a) CRA3FA and (b) CRA4FA; only top half of the samples was imaged (in black frames).

4. Reactive transport modelling

4.1. Modelling of the experiment cases

Figure 5 shows the calcite precipitation patterns and the associated permeability evolution obtained in the simulations, with a satisfactory visual agreement compared to the experiments CRA3FA and CRA4FA (Figure 4), both regarding the amount of precipitation near the inlet and the difference in the extent of precipitation in the main flowpaths. A good agreement is also obtained with the experimental calcium outlet concentration and overall volume of precipitation (Figure 6), using an initial specific surface area, S_0, of 60 $m^2 \cdot l^{-1}$ and a precipitation-dependant term, S_{growth}, of 0.21 $m^2 \cdot g^{-1}$ for all the samples. The increase in specific surface area with precipitation further enhances the precipitation rate as far as the porosity decreases, thus explaining a slight decrease of $[Ca]_{out}$ with time. Nevertheless, the volume precipitated is a bit overestimated for CRA1FA and underestimated for CRA4FA. Although it is possible to obtain better fits by adjusting the specific surface area, we prefer to keep the same value for S_m to validate the model for the different geometries and flow conditions.

Modelling of experiment CRA1FA, which is equivalent to a simple 1D-model, allows for examining specifically the kinetic model, which depends on both the kinetic formulation (Eq. 10) and the evolution of the specific surface (Eq. 11). For all cases explored, a good agreement is found between experiment and simulation regarding the volume fraction of calcite precipitated along the flow path, except near the inlet boundary, where uncertainties remain (Figure 7). Reducing S_0 to 8 $m^2 \cdot l^{-1}$ with no precipitation-dependant surface area (i.e., S_{growth} =0) would decrease the amount of calcite precipitated near the inlet and permit to better fit with the total amount of calcite precipitated (4.4 mm^3 *vs* 3.1 mm^3 in Table 3). A lower S_m would also highlight the drop in precipitation rate linked to $\Omega_{crit,dol}$ which occurs at x ~ 8 mm from the inlet, where the gradient of precipitation is less pronounced. In addition, taking a constant specific surface area through the simulation (i.e., $S_m = S_0$) would also largely modify the amount of calcite precipitated near the inlet compared to a variable specific surface area (i.e., $S_m = S_0 + S_{growth}$) (Figure 7). For instance, increasing the value of S_{growth}, from 0 to 0.21 $m^2 \cdot g^{-1}$, results in a larger increase of precipitation near the inlet, promoting the reduction in permeability and sealing of the fracture. However, it is worth noting that the behavior near the inlet is difficult to assess as: (i) part of the sample inlet surface is also exposed to the inlet fluid in the experiment and (ii) the simulation critically relies on the models for reactive surface area and permeability evolution, limiting the evaluation of the kinetic model.

The local changes in porosity and permeability significantly affect the flowpaths through time, through a negative feedback between flow and transport (Supplementary video S1). Reactive fluid is initially focused within the areas of higher apertures, i.e. the main flow paths, where the precipitation rate is higher. Indeed, a higher renewal rate of the inlet fluid maintains a higher saturation index along the preferential flowpaths. Preferential filling of these flowpaths with calcite decreases locally the permeability, thus leading to a progressive reorganization of the flow in areas initially deserted by the fluid, whose permeability becomes at some point higher than the permeability in the filled flowpaths.

Experiment CRA2FA at low flow rate is the most efficient from the point of view of calcium uptake from the inlet fluid, in the sense that the overall calcite precipitation was reduced only by a factor 8-10 compare to high flow rate, while the calcium flux at the inlet boundary ($F_{Ca} = Q_0 \times [Ca]_{in}$) is comparatively 30 times lower. This is explained by the longer resident time, which favors a higher consumption of calcium along the fracture. However, in result, precipitation is more localized near the inlet (Figure 5a) compare to high flow rate (experiment CRA3FA).

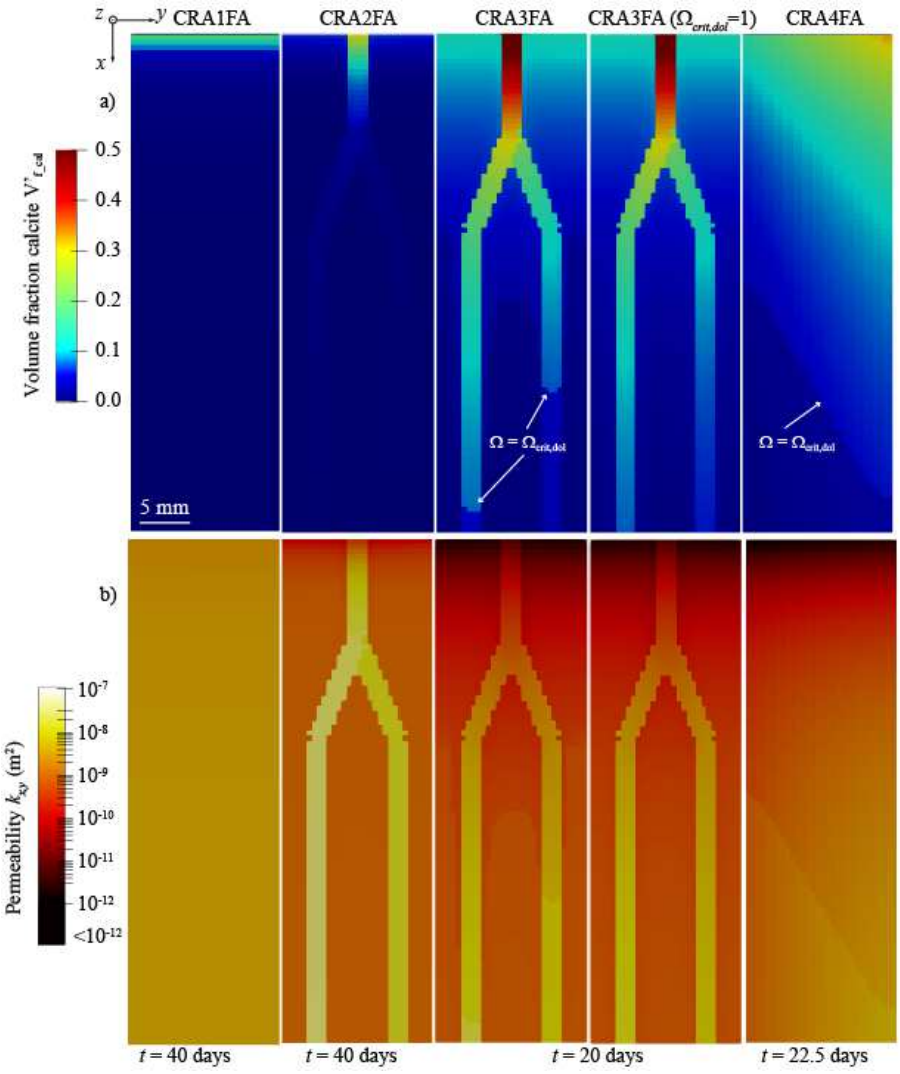
Interestingly, the simulations are able to reproduce the sealing observed experimentally. When porosity reaches low values (below 5%), prediction of sealing becomes strongly dependent on the empirical porosity-permeability relationship, and on the choice of a critical porosity or permeability. S_{growth} plays also an important role by promoting precipitation where precipitation is more important, i.e. near the inlet. In the simulations, almost complete sealing is assumed when fracture aperture is reduced to about 4 µm near the inlet, like in the experiments, thus corresponding to permeability decreases by 5 orders of magnitude. Given that threshold, sealing at the inlet of CRA3FA and CRA4FA is almost completed after 20 and 22.5 days, respectively (Figure 5b). A further decrease in permeability by 9 orders of magnitude is reached after 23 and 25 days, respectively. It is worth noting that the geometry of the fracture plays an import role on the time required for sealing. For instance, CRA3FA is unexpectedly sealed earlier than CRA4FA despite a larger maximum aperture (700 versus 400 µm), while mean apertures were comparable (280 ± 5 µm). In other words, large aperture flow channels with high reactant flux fill more rapidly than areas of low aperture.

Simulations also permit to account for different precipitation conditions onto the two mineral substrates (Figure 5a). Initially, the specific surface area is the same for calcite and dolomite ($S_{cal} = S_{dol}$). When considering a critical saturation state $\Omega_{crit,dol}$, there is a point beyond which the fluid is not sufficiently oversaturated to initiate precipitation on the dolomite substrate. This results in a slight discontinuity in the downstream calcite precipitation pattern compared to the case $\Omega_{crit,dol} = 0$ (Figure 5a,

549 cases CRA3FA), as well as a lower precipitation rate. Difference in the two approaches mostly affects
550 downstream calcite precipitation patterns with no effect near the inlet boundary.

551

552



553

554 Figure 5. Modelling of the (a) volume fraction of calcite precipitated and (b) permeability field in the
555 four fracture geometries using $\Omega_{crit,dol}$ = 10, and comparison with $\Omega_{crit,dol}$ = 1 for CRA3FA. For fractures
556 CRA3FA and CRA4FA, time corresponds to a five order of magnitude drop in $\langle k_x \rangle$.

557

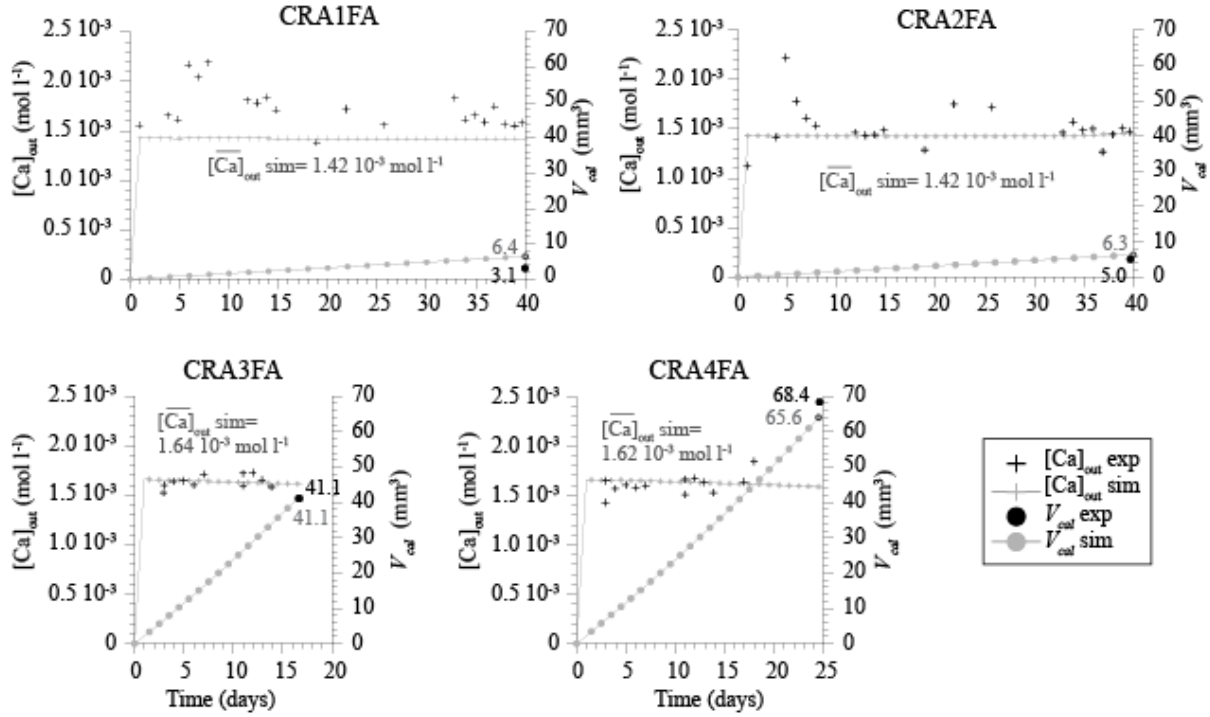


Figure 6. Experimental and modelling results of the temporal evolution of calcium concentration at the outlet $[Ca]_{out}$ and volume of calcite precipitated V_{cal} for the four fractures CRA1FA to CRA4FA. The same kinetic law and specific surface was used for modelling of the experiments (i.e., R_{cal} from Eq. 10, S_0 = 60 $m^2 \cdot l^{-1}$ and S_{growth} = 0.21 $m^2 \cdot g^{-1}$ for both calcite and dolomite, and $\Omega_{crit,dol}$=10). The average calcium concentration at the outlet obtained in the simulations ($[\overline{Ca}]_{out}$), and the volume of calcite calculated from mass balance (black) and from modelling (grey) are also indicated in the graphics.

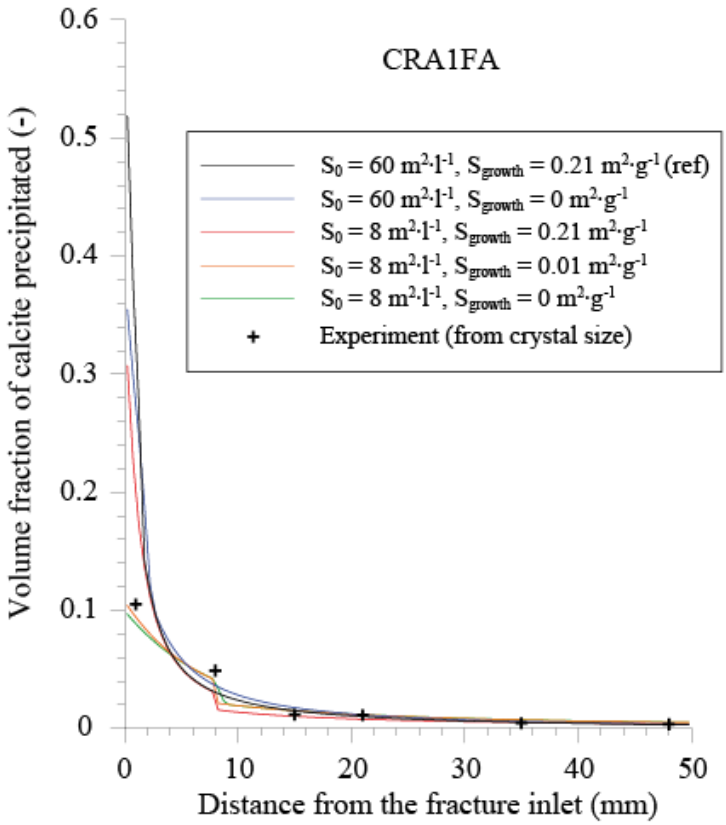


Figure 7. Evolution of the volume fraction of calcite precipitated along the flow path in fracture CRA1FA for different specific surface area models (i.e., different values of S_0 and S_{growth}), and comparison with data derived from SEM observations. The drop of precipitation at about x = 8 mm underlines the limit of precipitation onto dolomite, i.e., $\Omega_{cal} = 10$.

4.2. Modelling of the synthetic fractures

The reactive transport approach is then applied to the synthetic fractures, in order to generalize the experimental observations to fracture geometries more relevant of the ones encountered in natural systems.

4.2.1. Effect of reactive transport conditions

For the range of precipitation and flow rates tested in the simulations, we observe very different precipitation patterns (Figure 8). Two different regimes, similarly to those described in the literature, are identified depending on the value of $Da_{adv,0}$, i.e. non-uniform compact precipitation and quite uniform

580 precipitation [36]. Precipitation is predicted to be compact, i.e., highly localized at the inlet, for the highest
581 values of $Da_{adv,0}$ (30-300β), whereas it is more uniform along the flow paths for the lower values of
582 $Da_{adv,0}$ (0.1-0.3β).

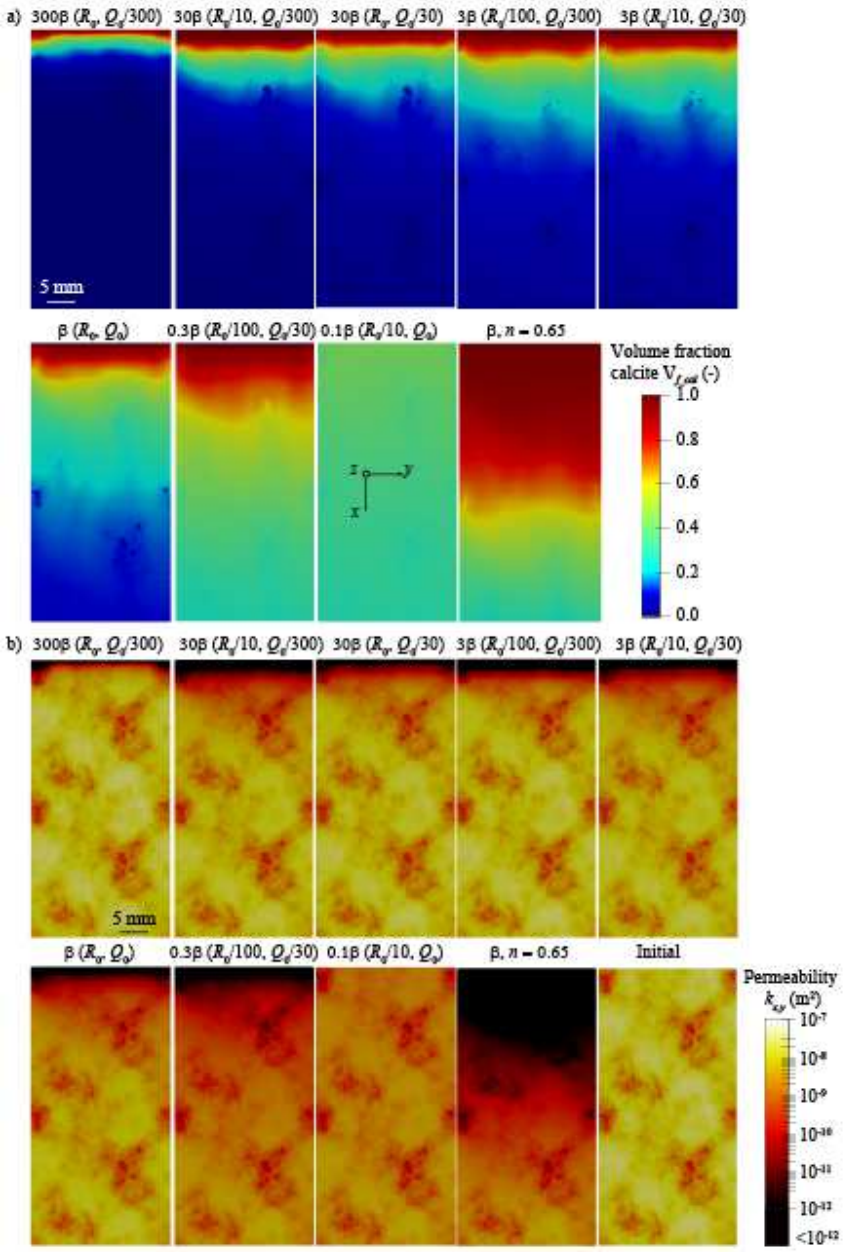
583 At high $Da_{adv,0}$, precipitation is focused near the inlet and the solution becomes rapidly depleted in
584 reactants, leading to compact precipitation. The rapid precipitation has a positive feedback on reactivity by
585 increasing the specific surface area near the inlet, favoring sealing potential. For $Da_{adv,0}$=300β, log Ω_{cal}
586 drops from 1.38 to 0.2 in the first millimeters, and equilibrium is reached within the fracture. Precipitation
587 starts in the main flow paths, whose rapid filling leads to a quick reorganization of the flow at the inlet. As
588 a result, sealing of the fracture is quick, and happens for a low amount of calcium injected (<0.01 mol)
589 and an average porosity reduction of less than 5%.

590 At low $Da_{adv,0}$, precipitation is more uniform in the fracture void, especially for reactivity factors
591 {RF<1, n=1.12}, for which Ω_{cal} decreases by less than one unit through the fracture. In the case {RF=1,
592 n=0.65}, the lower dependence of the precipitation rate to the saturation index allows for more uniform
593 precipitation along the fracture void as well. As a result, complete sealing of the fracture is expected to be
594 quite slow but uniform, and should only happen for a large amount of calcium injected, as evidenced by
595 an effective permeability reduction in the flow direction ($\langle k_x \rangle$) of less than one order of magnitude for a
596 10% global-porosity reduction.

597 Similar values of $Da_{adv,0}$ but one order of magnitude difference in both Da_0 and Pe_0 (i.e., for $Da_{adv,0}$
598 = 3 and 30β) do not lead exactly to the same precipitation patterns. Indeed, for a similar porosity
599 decrease, permeability reduction is higher for the highest values of Da_0 and Pe_0.

600 While sealing of the fracture is expected at some point, it is worth noting that changes of the effective
601 permeability parallel ($\langle k_x \rangle$) or perpendicular ($\langle k_y \rangle$) to the flow direction can be very different (Figure 9).
602 For the uniform precipitation regime, $\langle k_x \rangle$ and $\langle k_y \rangle$ decrease in the same ratio. In contrast, for the
603 compact precipitation regime, $\langle k_x \rangle$ can decrease 5 orders of magnitude while $\langle k_y \rangle$ is reduced by only
604 10%, due to localization of precipitation at the inlet boundary. The high discrepancies are the expression
605 of the non-uniform precipitation at the fracture scale.

606



607

608 Figure 8. (a) Volume fraction of calcite precipitated in the fracture void and (b) associated permeability
609 evolutions observed for different values of $Da_{adv,0}$ in the synthetic fracture with {AF=1; //} and n = 1.12.
610 The case with n = 0.65 and the initial permeability field are also presented. Note that sealing has not been
611 reached yet for the case 0.1 β.

612

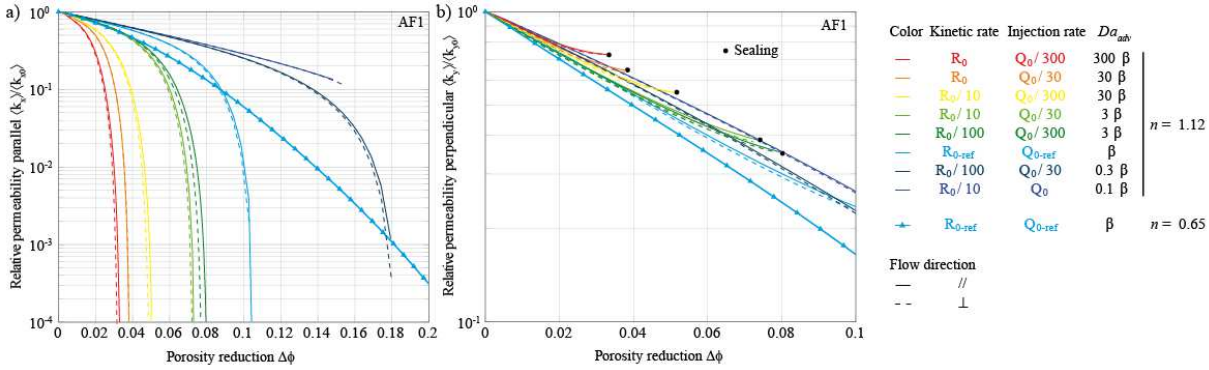


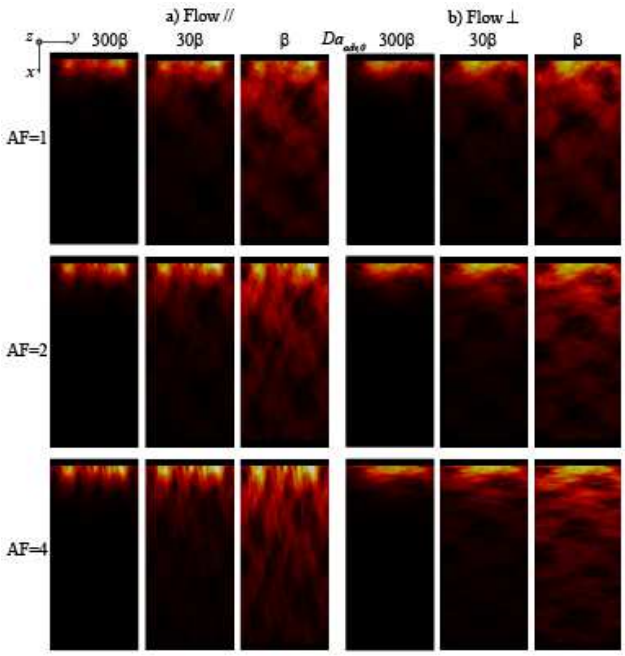
Figure 9. Evolution of the relative effective permeability (a) parallel ($\langle k_x \rangle / \langle k_{x0} \rangle$) and (b) perpendicular ($\langle k_y \rangle / \langle k_{y0} \rangle$) to the flow direction as a function of porosity reduction $\Delta\phi$. The geometries used in the simulations are {AF = 1; //} (solid lines) and {AF = 1; ⊥} (dotted lines), with n = 1.12. The different curves stand for the different values of $Da_{adv,0}$. The case with n = 0.65 is also presented and underlines a very different porosity-permeability path than the reference case with n = 1.12.

4.2.2. Effect of fracture and flow anisotropy

Figure 10 shows the effect of the geometric anisotropy factor with regards to the flow direction {AF = 1, 2 or 4; // or ⊥} on the precipitation patterns and permeability reduction. Increasing anisotropy has only slight but opposite effects depending on the stretching direction of the aperture field. Stretching parallel to the flow direction (//) both decreases the tortuosity of the flow paths and increases the longitudinal dispersivity [102], thus spreading the high reactive fluid over longest distances. As a result, precipitation is a little less localized at the inlet and more uniform along the flow paths. Local precipitation-induced aperture reduction promotes the reorganization of flow paths. Precipitation being localized initially in the regions of higher porosity, this has a net effect in reducing the fracture anisotropy, but only at the low $Da_{adv,0}$ (Figure 10). In contrast, aperture field stretching perpendicular to the flow direction (⊥) increases the tortuosity of the flow paths, thus increasing the residence time of the reactants and favoring precipitation and sealing near the inlet boundary. Changes in effective permeability parallel or perpendicularly to the flow direction (Figure 11) suggest only a slight impact of the orientation of the fractures with regards to the flow direction for most $Da_{adv,0}$, with the // and ⊥ permeability reduction curves getting more separated with increasing anisotropy factor (Figure 9 and Figure 11). No impact is noticed at high $Da_{adv,0}$ where the rapid sealing at the inlet occurs whatever the fracture aperture field heterogeneity.

637 For the other values of $Da_{adv,0}$, whereas the permeability reduction curve is barely affected in the
638 isotropic case (Figure 9), increasing AF enhances the impact of fracture orientation to the permeability
639 evolution (Figure 11).

640



641

642 Figure 10. Evolution of the precipitation patterns in fractures of different anisotropy factor and flow
643 direction {AF = 1, 2 or 4; // or ⊥} for different values of $Da_{adv,0}$ (β, 30β, and 300β). Flow is (a)
644 parallel or (b) perpendicular to the direction of stretching of the fracture aperture field.

645

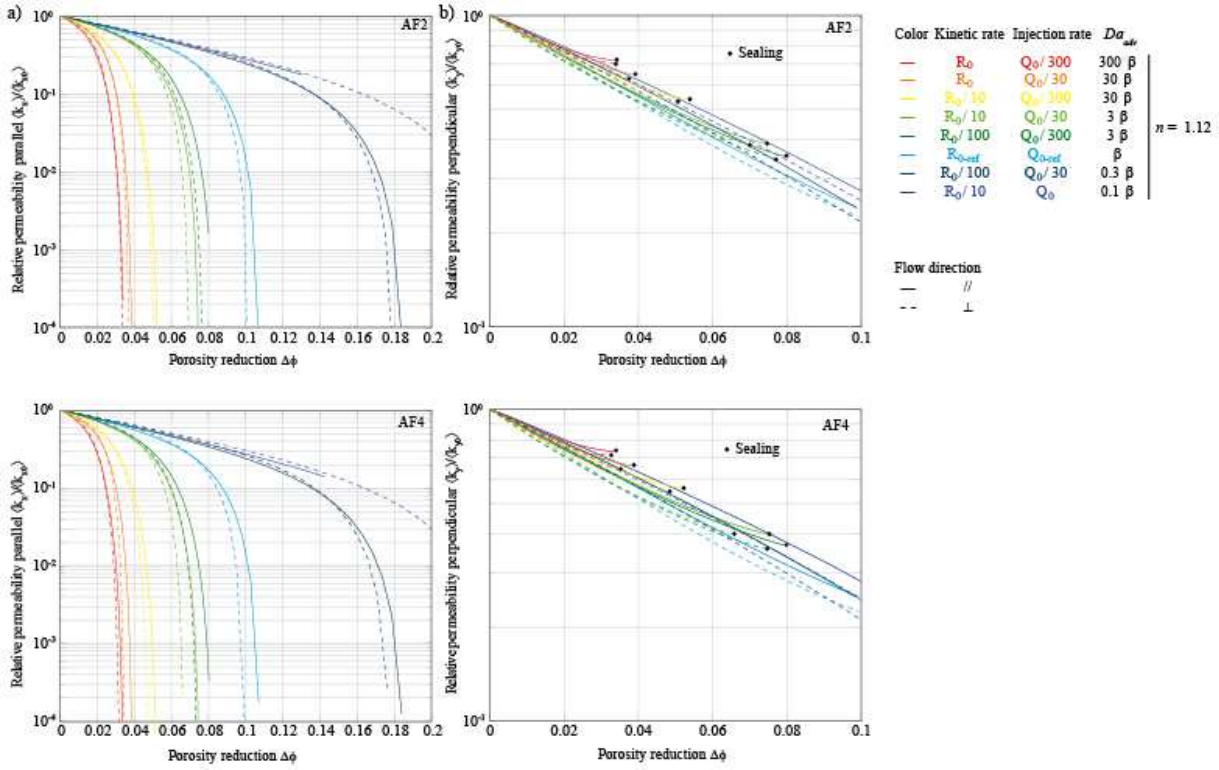


Figure 11. Evolution of the relative effective permeability (a) parallel ($\langle k_x \rangle / \langle k_{x0} \rangle$) and (b) perpendicular ($\langle k_y \rangle / \langle k_{y0} \rangle$) to the flow direction as a function porosity reduction for different anisotropy factors and flow orientations {AF = 2, 4; // or ⊥}, and $Da_{adv,0}$ values.

4.2.3. Effect of mineral heterogeneity at the fracture walls

For the range of mineral substrate distributions at the fracture wall (Masks 1 to 3 and inv-Mask 2 and 3) and critical saturation state ($\Omega_{crit,dol}$ = 10, 20 and 30) tested in the simulations, we observe evolutions of fracture geometry (Figure 12) and permeability (Figure 13) very different from the case calcite and dolomite substrates are set as a continuum. The geometry and permeability evolutions are highly dependent of both $\Omega_{crit,dol}$ and the spatial distribution of mineral substrates.

Using the continuum description for mineralogy (i.e., 50-50 calcite dolomite in every mesh) and in the condition of simulation {AF = 4; //} and $Da_{adv,0} = \beta$, increasing $\Omega_{crit,dol}$ restricts the fraction of fracture void where precipitation will occur onto dolomite substrate. There is a limit at a certain distance from the inlet from which precipitation onto dolomite stops, thus decreasing the amount of precipitated calcite

661 downstream. However, precipitation near the inlet remains equivalent to what happens when no restriction
662 is set for precipitation onto dolomite substrate (i.e., $\Omega_{crit,dol} = 1$), except in the case $\Omega_{crit,dol}$ = 30, for
663 which precipitation is reduced to about a factor two at the inlet, inherent to the fact $\delta(a)$ returns 0 in
664 Eq.10. As precipitation is localized near the inlet, $\langle k_x \rangle$ evolution remains quite similar for the different
665 cases and it does not either affect the sealing capacity of the fracture. In the same way, $\langle k_y \rangle$ is barely
666 affected.

667 In contrast, using the heterogeneous distribution of mineralogy with the different masks prevents
668 precipitation from happening onto dolomite through part or totality of the fracture void, i.e, in every
669 100%-dolomite meshes where $\Omega_{crit,dol} > \Omega_{cal}$. In that case, the precipitation patterns and permeability
670 evolution are highly dependent on the spatial distribution of mineral heterogeneity and the spatial
671 continuity of the non-reactive substrate.

672 Increasing $\Omega_{crit,dol}$ enhances the heterogeneity of both precipitation and flow downstream, but
673 precipitation is not affected upstream (Figure 12,b). No precipitation onto dolomite has two consequences.
674 First, the fluid keeps a higher saturation index, allowing precipitation to progress further in the fracture
675 void. However, the porosity reduction remains, slower, as between 0 and 50% of the surface area in the
676 domain is not reactive anymore, explaining a more rapid drop in permeability with porosity reduction
677 when $\Omega_{crit,dol}$ increases from 10 to 20 (Figure 13).

678 Taking the critical case $\Omega_{crit,dol}$ = 30 as an example, i.e. no precipitation onto dolomite through the
679 whole domain, we clearly see the differences between the different masks of heterogeneity in term of
680 precipitation patterns, permeability evolution, and reorganization of flow (Figure 12,c-f and
681 Supplementary video S2). Precipitation only happens onto calcite and starts in high aperture areas hosting
682 this substrate. Filling of these areas progressively drives the flow to areas where no precipitation is
683 possible, creating new flow paths independently of the negative feedback between flow and transport
684 observed in the case precipitation is not restricted to one mineral phase. In particular, if the dolomite
685 substrate is continuous in the flow direction (i.e., for inv-Mask2), sealing will be impossible and the
686 effective permeability $\langle k_x \rangle$ decreases only slightly to reach a limit $\langle k_x \rangle_{\lim}$ (Figure 13). Consequently,
687 permeability cannot decrease further and flow stabilizes to a steady state. In contrast, if the dolomite
688 substrate is not continuous, flow will stop once precipitation onto calcite forms a barrier to flow (i.e. for
689 Mask 1 and inv-Mask 2). The aperture-correlated clusters (Mask3 and inv-Mask3) are interesting in the
690 sense that the dolomite substrate is continuous in both cases, so that no sealing is possible. However, the

evolution of permeability is different depending on whether calcite is set in the large-aperture fraction (Mask3) or low-aperture fraction (inv-Mask3). In these cases, flow is naturally driven towards the main channels of larger aperture. For the case Mask3, they contain a substrate of calcite. As a result, the channel inlets fill rapidly with calcite, thus provoking a more rapid permeability decrease with porosity reduction than inv-Mask3, up to the point the flow is diverted to the low-aperture channels with a dolomite substrate. In this case, precipitation results in a large reorganization of flow. Precipitation being impossible onto dolomite, permeability stabilizes whereas precipitation continues downstream on the calcite substrate (Supplementary video S2). In contrast, for inv-Mask3, there is no precipitation in the main flow channels, which contains dolomite. Calcite precipitation is still maintained in areas adjacent to the main channels through diffusion-transverse dispersion, but is slower. Consequently, high saturation are maintained over longest distances and permeability decreases more smoothly with porosity reduction (Figure 13a), although the drop is larger as a function of time than for Mask3 (Figure 13b).

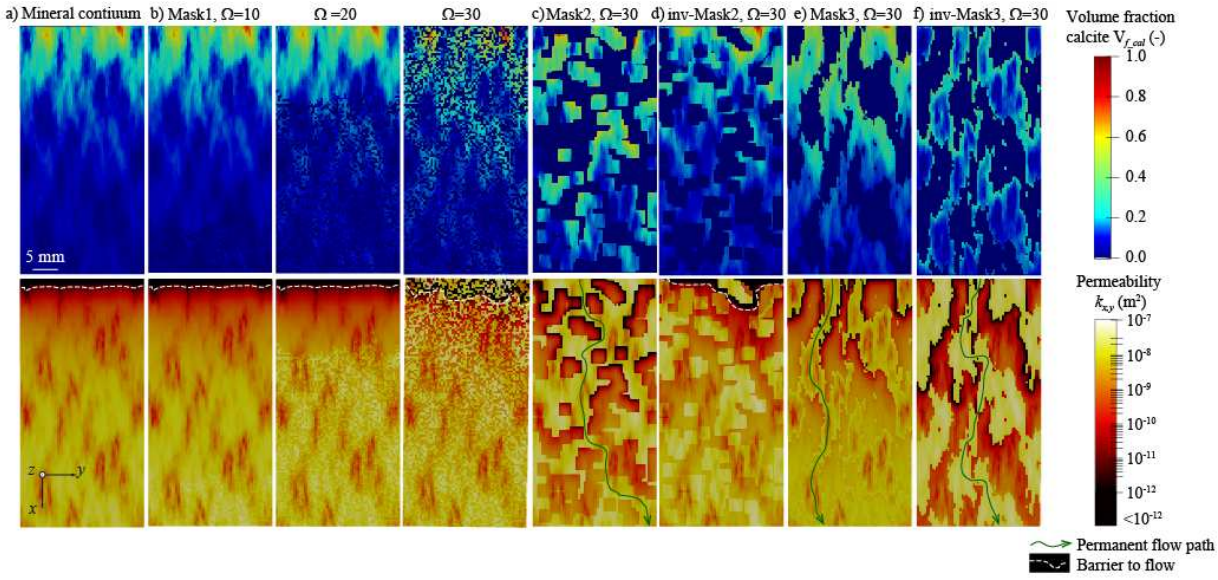
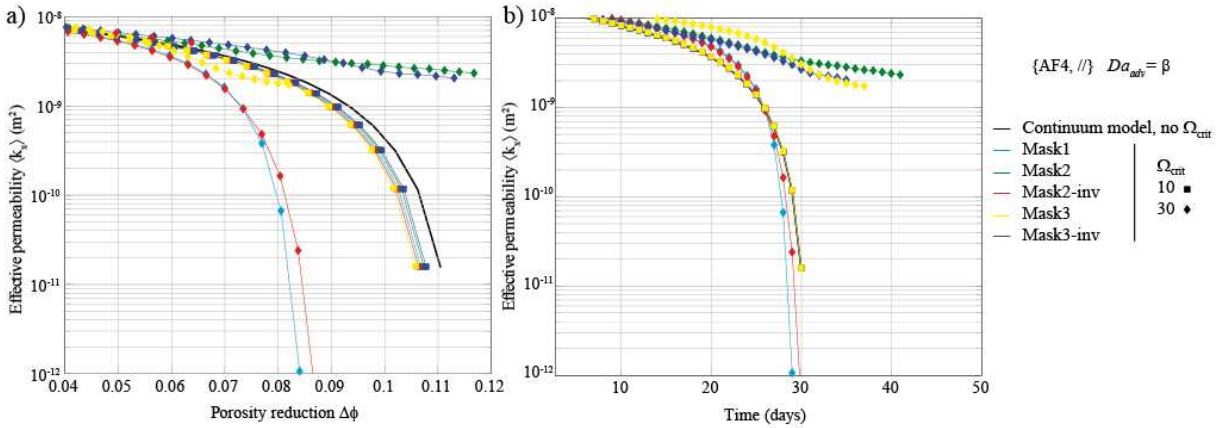


Figure 12. Evolution of the calcite precipitation patterns and permeability in synthetic fractures with different mineral heterogeneity distribution at the fracture walls, and for different critical saturation states $\Omega_{crit,dol}$: (a) reference case with 50-50 calcite dolomite in a continuum; (b) small randomly generated clusters (Mask1); (c-d) large randomly generated clusters (Mask2 and inv-Mask2), calcite and dolomite fractions are switched between the two cases; (e-f) aperture-correlated clusters (Mask 3 and inv-Mask3); for Mask3 (e), calcite occupies the larger fracture void fraction mimicking alteration of the fracture prior to precipitation; (f) is the complementary case (inv-Mask3). The fractures have an anisotropy factor and

712 flow orientation (AF = 4; //), and $Da_{adv,0} = \beta$. The barriers to flow and the persistent flow paths are
713 underlined in the figure.
714



715

716 Figure 13. Evolution of the effective permeability parallel to the flow direction $\langle k_x \rangle$ with (a) porosity
717 reduction or (b) time and as a function mineral heterogeneity distribution at the fracture walls and critical
718 saturation states ($\Omega_{crit,dol}$ =10 or 30). Comparison with the continuum case (no $\Omega_{crit,dol}$). The fractures
719 have the anisotropy factor and flow orientation {AF = 4; //} and $Da_{adv,0} = \beta$.

720 ## 5. Discussion

721 ### 5.1. Precipitation process and reorganization of flow

722 The precipitation regime strongly depends on $Da_{adv,0}$. At a given flow rate, however, the compact
723 precipitation regime is also largely dependent on the shape of the kinetic rate law [51], which is itself a
724 function of the saturation index. Far-from-equilibrium conditions (log Ω_{cal} > 0.8) will promote three-
725 dimensional growth of islands or two-dimensional surface nucleation at the mineral surface. These growth
726 regimes result in high values of the exponent n > 2, [52] that will accentuate the strong drop of
727 precipitation at the inlet as far as the reactants are consumed. In contrast, for moderate saturation indexes
728 (log Ω_{cal} < 0.8), the spiral growth mechanism results in an exponent n~1. [52]. In this case, the drop in
729 precipitation rate with the saturation index is less sharp, especially near the equilibrium (i.e., when
730 $1-\Omega \to 0$) where the precipitation rate is almost constant. This would result in relatively uniform
731 precipitation along the flow path. Testing an n ~ 0.65 (i.e., precipitation rate poorly dependent of the

saturation state), although the assumption is far-fetched for mineral precipitation driven by injection of oversaturated fluids, confirms the importance of the fluid reactivity path in the reorganization of flow.

The effect on the specific surface area increase with precipitation can also promote the compact precipitation regime. Introducing a specific surface area dependant to the amount of new precipitate (Eq. 12) clearly shows a positive feedback loop, thus contributing to a faster sealing near the inlet. The value of 0.21 $m^2 \cdot g^{-1}$ for S_{growth} used in the simulations is questionable as it was obtained during precipitation onto calcite seeds. No evident decrease of $[Ca]_{out}$ with time supports a large increase in specific surface area during precipitation, although the sensibility in determining ΔCa from chemical analyses is low for precipitation studies. Whatever the extent of S_m increase, it should have large consequences on the evolution of precipitation patterns and time for sealing. Under constant S_m conditions, closure of the fracture would normally drive fluid with a higher supersaturation index further in the fracture void, as a result of fluid velocity increase. However, when S_m increases and despite the fluid velocity increase, precipitation remains localized near the inlet. This is particularly visible when looking at the level sets of Ω_{cal}: they move upward in the fracture as the reaction rate increases near the inlet (see supplementary videos S1 and S2). As a result, an increase in S_m promotes as well the compact precipitation regime as well.

It is clear that the lack of constrains on the kinetic formulation is the primary source of uncertainty for modelling reactive transport and predicting the time required for complete sealing. Nevertheless, these observations confirm that $Da_{adv,0}$ cannot solely be an indicator for the reaction regime [53], as evolution of the local precipitation rate through time, along the flow paths, and through the fracture, is a time- and space-dependant process.

5.2. The importance of mineral substrate heterogeneity

Both the experiments and simulations have evidenced the role of mineral substrate distribution at the fracture walls on the evolution of fracture geometry and flow reorganization. The modelling results show that mineral heterogeneity can have a profound impact, larger than that of $Da_{adv,0}$ or fracture geometry, on the precipitation regime, reorganization of the flow and sealing capability. It will both depend on the spatial distribution of substrate clusters and on the ability for new crystals to grow at their surface, in relationship with the critical saturation index ($\log \Omega_{crit}$).

Modelling with mineral spatial heterogeneity has shown that dolomite substrate –or more generally any mineral phase whose surface energy is different from the primary mineral– can significantly alter the

762 filling of the fracture void. In case precipitation is restrained or not permitted in specific fracture regions,
763 the spatial connectivity or, conversely, the absence of connectivity of the non-reactive substrate, will
764 underling two extreme cases of permeability evolution, with either (i) a rapid drop in permeability and
765 fracture sealing for small and spatially non-connected mineral spots (Figure 13), or, in contrast, (ii) only a
766 slight decrease of permeability that stabilizes, when the non-reactive substrate is connected through the
767 void space.

768 Consequently, the presence of substrate clusters can change the precipitation regime. For small, non-
769 connected clusters, the regime can be more compact. In contrast, for non-reactive substrate connected
770 through the fracture, sealing might never be reached. Indeed, large-scale portions of the fracture void can
771 fill up while flow is ultimately maintained in the network of non-reactive substrate. In absence of
772 precipitation onto that substrate (i.e., when $\Omega_{crit} > \Omega_{cal,0}$), some flow paths will remain free of
773 precipitation, thus preventing fracture sealing. Although not investigated in this study, the proportion (%)
774 of non-reactive mineral substrate at the fracture wall is certainly a key parameter that will control fracture
775 spatial connectivity.

776 The concentration field of reactants and precipitate in the reactive and non-reactive paths will also be
777 largely dependent on the mineral substrate heterogeneity. This is important for environmental studies, e.g.
778 when a contaminant is expected to be stabilized in a mineral phase (e.g., [103, 104]) or for biogrouting.
779 Not only the capacity of sealing will be affected, but the propagation distance of the chemical species will
780 highly depend on the mineral substrate heterogeneity.

781 The modelling underlines the limits of the continuum approach in this context of selective precipitation
782 onto a specific mineral phase, as it does not resolve the possible connectivity of the mineral substrates in
783 space. This also agrees with the conclusion of [105], that the continuum model, by averaging properties
784 and representing the system as if it is well mixed, does not resolve the pore-scale structure when high
785 concentration gradients develop. Although their conclusions were reached for dissolution of minerals with
786 a high contrast in reactivity, this can be extended to precipitation involving mineral substrates with
787 different surface energy or affinity with the new precipitate. However, for precipitation, mineral
788 heterogeneity might prevent from sealing only when the non-reactive substrate forms a connected
789 network, maintaining flow paths open for the reactive fluid. In addition, it is expected that the
790 phenomenon is transient in reality, as the model does not account for possible lateral growth of crystals
791 that could finally cover the non-reactive clusters at some point, like observed experimentally near the
792 fracture inlets. Bridges made between newly grown crystals might compensate for heterogeneous
793 distribution of mineral substrate heterogeneity at the fracture walls.

In any case, mineral heterogeneity should nevertheless promote a more uniform filling of the fracture, when possible, although we do not know yet whether the grain boundaries between the growing crystals and the non-reactive substrate mineral will remain or not micro-porous and possibly connected.

Flow channelization is also highly sensitive to mineral spatial distribution in rocks. The negative feedback between reaction and flow tends to minimize local perturbations, whereas precipitation localized on a specific substrate tends to magnify them. The flow properties, which are highly dependent of the spatial reduction of fracture aperture, are therefore largely modified by the presence of mineral heterogeneity. In this case, the continuum approach would fail at describing the reorganization of flow and the persistence of open flow paths.

5.3. Evolution of the effective porous medium properties and implications for fracture sealing

For engineering purposes, reactive transport simulations often require large spatial scale models, which rely on upscaled properties of the porous/fractured media when subject to mineral dissolution/precipitation reactions. Hence, pore or fracture-scale micro-continuum simulations can be useful to better assess the evolution of the medium properties, and feed continuum models with upscaled properties.

When precipitation occurs with no distinction of mineral substrate, the extent of the porosity and permeability alteration, and the porosity-permeability relationship are highly dependent on Da_{adv}, although this parameter alone might not be sufficient to fully describe fracture sealing. For instance, Ahkami et al. [74], who isolated different precipitation regimes in fractured porous media, must refer to both Da_0 / Pe_0 and Pe_0 to define these regimes. In addition, it is difficult to provide a numerical value for Da_{adv} when regarding heterogeneous phase reactions, like mineral precipitation [53], so that we preferred to explore the effect of $Da_{adv,0}$ relatively to a reference parameter, i.e., β. The way the fracture can be sealed uniformly, i.e., associated to a permeability reduction both along and across the main flow directions, will depend on two factors: (i) the precipitation kinetics –in strong relationship with the saturation index and the specific surface area model–, and (ii) the mineral substrate distribution.

From our results, it appears that only slow (i.e., long-term) precipitation in conditions close to the equilibrium can guarantee proper sealing of fractures over large scales, something required to ensure reservoir tightness and improvement of the mechanical properties of fractured rocks (e.g., recovering cohesion, [8, 69]). High fluid velocities could help to obtain a similar result as well, although the strong non-linear decrease in precipitation kinetics of highly saturated fluids will be an obstacle to uniform fracture sealing, as well as a possible increase of specific surface of minerals through precipitation. In any

825 case, the ratio of the critical porosity, defined as the porosity below which the fracture is sealed (i.e.,
826 $\phi_c = \lim_{\langle k_x \rangle \to 0} \phi$) to the initial porosity, i.e., ϕ_c / ϕ_0, can be a good indicator of the fracture sealing efficiency.
827 The critical porosity increases with decreasing $Da_{adv,0}$, and at a given $Da_{adv,0}$, it increases or decrease
828 slightly depending on the anisotropy factor and flow orientation. A high ϕ_c / ϕ_0 will result in a small
829 fraction of the fracture void filled with calcite (i.e., compact precipitation), whereas a low ϕ_c / ϕ_0 will
830 indicate uniform sealing of the pore space (Figure 14).

831 When conditions for more uniform precipitation are encountered (i.e., for low exponent *n* or $Da_{adv,0}$),
832 the negative feedback between flow and transport will tend to decrease the permeability anisotropy of
833 fractures, so that at a larger scale the permeability in fractures can be described by an isotropic tensor.

834 In contrast, non-uniform compact precipitation driven by the non-linear precipitation rate and/or
835 coupling between flow and reaction will act as a barrier to flow in the vicinity of the injection point. This
836 regime has the highest impact on permeability reduction, and local sealing can be achieved quickly in far-
837 from-equilibrium conditions and high $Da_{adv,0}$ values. However, in that case, sealing will be restricted to a
838 narrow band near the inlet boundary, e.g., the injection well. Then, the negative feedback between flow
839 and transport will tend to increase the permeability anisotropy of fractures -whatever the initial anisotropy
840 factor or flow direction- by inducing a drastic reduction of permeability in the flow direction ($\langle k_x \rangle$)
841 whereas minor changes will be recorded transverse to the flow ($\langle k_y \rangle$). It is also difficult to decipher what
842 will happen further from the injection point, as non-uniform precipitation will trigger development of
843 anisotropic effective properties at larger scales, regarding for instance porosity and permeability, and
844 cause important large-scale reorganization of flow. It is possible the fluids are diverted in other channels
845 in the fracture, switched to adjacent partially-sealed fractures or that complete sealing compartmentalizes
846 large scale fluid flow like observed in geothermal reservoirs [10].

847 These conditions are only valid, however, when precipitates cover the entire surface of the fracture
848 walls. When polymineralic fracture walls are considered, mineral substrate heterogeneity and energy
849 barriers for precipitation can delay [106] or even prevent sealing, by reducing the specific surface area for
850 precipitation or locally inhibiting precipitate nucleation and/or growth. The persistence of a micro-porous
851 network resulting from heterogeneous precipitation distribution at the surface of the different mineral
852 substrates is also something to take into account, which could pinpoint the limits of unconstrained
853 continuum modelling. In particular, if precipitation is refrained from certain flow paths (Figure 12),
854 critical porosity or sealing could never be reached in the model, although in natural fractures lateral crystal
855 growth is also possible. In that case, permeability and porosity will reach a lower limit. The choice for a

porosity-permeability relationship will be critical, as classical relationship could be unable to represent results when the precipitation is not uniformly distributed through the porous network [107].

In addition, the choice of a unique porosity-permeability relationship at the continuum scale is debatable, even for a given geometry of fracture. Indeed, it was shown here to strongly depend on the injection conditions and on the mineral spatial distribution at the fracture walls. For a given rock fracture, upscaling of porosity-permeability at the continuum scale will rely on the hydro-chemical conditions along the streamlines, i.e. on the localization within the fractured domain. However, a coupled description of the problem using a micro-continuum model that fully accounts of mineral distribution, fracture geometry, flow description, fluid reactivity and possible feedback between chemistry, geometry and transport is definitely helpful to decipher the time- and space-dependent evolution of reactive transport in fractures as to estimate time for sealing.

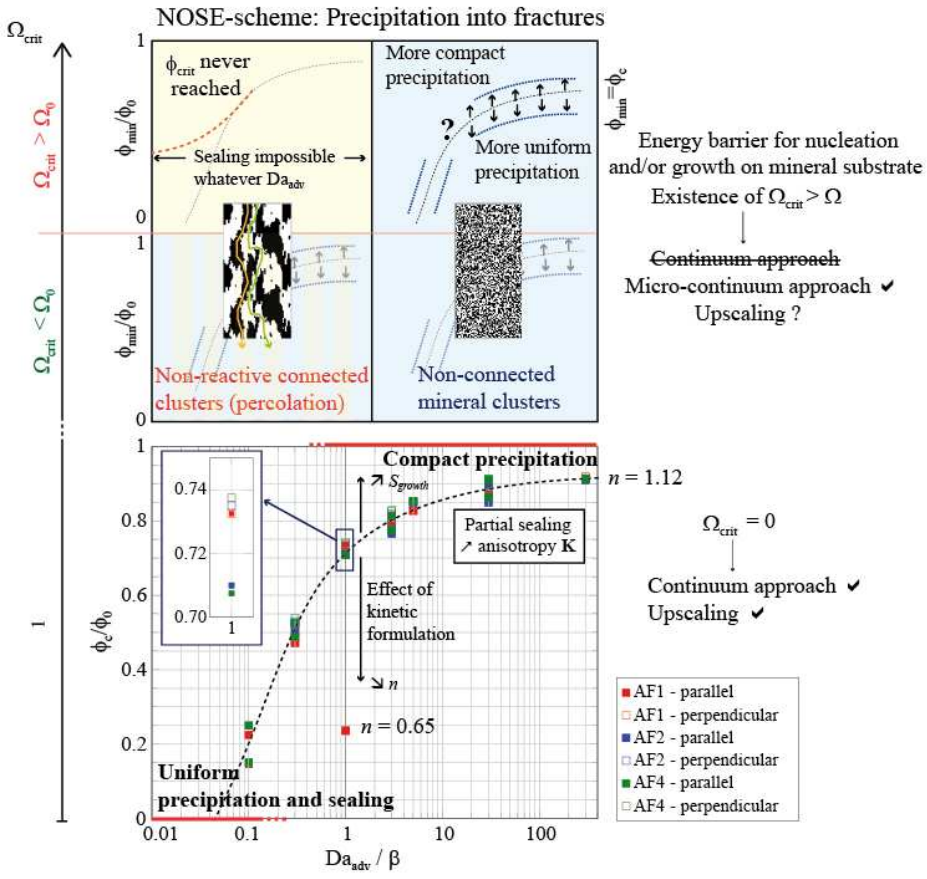


Figure 14. Critical porosity ratio ϕ_c / ϕ_0 as a function of $Da_{adv,0}$. The graphics underlines the influence of $Da_{adv,0}$ on the precipitation regime, but also show how the kinetic formulation, anisotropy factor, flow

871 direction, and critical saturation index with regard to the mineral substrate heterogeneity influence the
872 precipitation patterns and sealing capacity.

873 ## 6. Conclusion

874 We have presented a combination of experiments and reactive transport modelling to better
875 characterize the effect of mineral precipitation on the flow reorganization and sealing in fractures. In
876 particular, the impact of reactive transport driving forces (i.e., reaction *versus* flow), fracture geometry and
877 mineral heterogeneity distribution at the fracture walls was investigated. Simulations exploring several
878 flow rates, fracture geometries, precipitation rates, and distribution and reactivity of mineral substrates
879 which require a critical saturation state to initiate heterogeneous nucleation, Ω_{crit}, have been evaluated.

880 Contrary to dissolution, where a positive feedback between chemistry and flow can lead to a rapid
881 localization of flow along preferential pathways, precipitation tends to oppositely reorganize flow.
882 Precipitation is first promoted in the preferential flowpaths, where a higher saturation index and so a
883 higher precipitation rate are maintained further in the fracture void. Through a negative feedback between
884 reactions and transport, the flow is progressively diverted from the initial highly conductive channels and
885 reorganized until the fracture is sealed. Precipitation has shown to be non-uniformly distributed both in the
886 direction parallel and perpendicular to the main flow direction. Non-uniform precipitation along the flow
887 direction is related to the existence of main flowpaths that ensue both from the aperture field heterogeneity
888 and the fracture anisotropy factor, and to the balance between mineral reactivity and flow rate that can be
889 expressed through the initial advective Damköhler number, i.e., $Da_{adv,0}$. High $Da_{adv,0}$ favor a rapid
890 sealing near the inlet boundary, whereas low $Da_{adv,0}$ can lead to complete and uniform sealing of the
891 fracture. The nonlinear decrease in mineral precipitation rate for highly saturated fluids in far-from-
892 equilibrium conditions is a contributing factor to a rapid precipitation rate near the injection point. In
893 addition, when sealing is highly localized near the fracture inlet, it contributes to anisotropic permeability
894 increase, with $\langle k_x \rangle$ dropping quickly in the flow direction while little changes in $\langle k_y \rangle$ transverse to the
895 flow are observed. In contrast, uniform precipitation regime should contribute to decreasing the
896 permeability anisotropy of fracture exhibiting a high anisotropic factor.

897 Overall, the micro-continuum approach of reactive transport in fractures has shown the ability to
898 capture the major observations of the experiments. Calibration for one experiment (CRA3FA) showed the
899 model ability to make successful predictions for the results of other experiments under different flow rates
900 and fracture geometries, although much experiment effort is still required to better assess the kinetic law,

in particular, with regard to the evolution of the specific surface of growing crystals. These simulations show that a properly parameterized reactive transport model can reproduce precipitation patterns observed in anisotropic fractures, even close to complete sealing. At larger scale, the fracture anisotropy does not appear as an obstacle for a 1D continuum description of fractured media during precipitation process, as filling of the preferential flow paths will trigger transversally a reduction in aperture distribution heterogeneity with time. However, the continuum description at a larger scale could fail to describe the precipitation process of minerals of various affinities to mineral substrates, at least in the short term and for large-scale mineral substrate heterogeneity and connectivity, i.e. when all the fracture wall surfaces have not been yet covered by the new precipitate. The mineral substrate distribution definitely appears as an important factor that will drive the reorganization of flow with precipitation, in particular when both mineral clusters are big (in the *x*- and *y*- directions) regarding to the fracture aperture and connected through a network, and a high critical saturation index restricts precipitation on some substrates at the fracture walls. It is also probable that the role of mineral distribution, i.e. the rock texture, dominates over $Da_{adv,0}$ or fracture geometry anisotropy for prediction of the fate of reactive fluids in geological reservoirs or aquifers. It could constitute a new assumption to explain why fractures in shallow-depth environments are only partially filled with cement deposits and do not seal totally.

At larger scale and considering a fracture network, the increase in anisotropy of permeability can also lead to more complex reorganization of flow compared to what has been observed in this study. These simulations also suggest that pore-scale heterogeneities and anisotropy can exert a control on the distribution of the precipitates and hence on the evolution of the fractured medium properties. Application to natural systems exhibiting a high degree of heterogeneity in material properties (e.g. local porosity and permeability, mineral reactivity, specific surface area), will make these predictions more challenging. The study points at future models that could better include rock textures and mineral spatial distribution to improve their reliability. Nevertheless, the model remains a useful and computationally efficient tool to probe the interplay between precipitation reactions, flow and transport in rocks with complex mineral textures.

Acknowledgments

We would like to thank Laurent Auberoux (CM Quartz) for providing access to the Crayssac quarry, Jérôme Sterpenich (GéoRessources Nancy), Christophe Tenailleau and Benjamin Duployer (CIRIMAT Toulouse) for XMT acquisitions. We are also grateful for the SEM technical support provided by Philippe Recourt (Université de Lille 1) and Thierry Aigual (GET). C. Noiriel acknowledges funding from CNRS INSU through the project Tellus-CESSUR GEORAC.

References

[1] Noiriel C, F Renard, ML Doan, JP Gratier. Intense fracturing and fracture sealing induced by mineral growth in porous rocks. Chem Geol. 269 (2010) 197-209, doi: 10.1016/j.chemgeo.2009.09.018.

[2] Detournay E. Propagation Regimes of Fluid-Driven Fractures in Impermeable Rocks. International Journal of Geomechanics. 4 (2004) 35-45, doi: doi:10.1061/(ASCE)1532-3641(2004)4:1(35).

[3] Chen Y, Y Nagaya, T Ishida. Observations of Fractures Induced by Hydraulic Fracturing in Anisotropic Granite. Rock Mechanics and Rock Engineering. 48 (2015) 1455-61, doi: 10.1007/s00603-015-0727-9.

[4] Engelder T, A Lacazette. Natural hydraulic fracturing. in: N Barton, O Stephansson, (Eds.). Rock joints. A.A. Bakelma, Rotterdam, 1990. pp. 35-44.

[5] MacQuarrie KTB, KU Mayer. Reactive transport modeling in fractured rock: A state-of-the-science review. Earth-Science Reviews. 72 (2005) 189-227.

[6] Dobson PF, TJ Kneafsey, EL Sonnenthal, N Spycher, JA Apps. Experimental and numerical simulation of dissolution and precipitation: implications for fracture sealing at Yucca Mountain, Nevada. Journal of Contaminant Hydrology. 62-63 (2003) 459-76.

[7] Morrow CA, DE Moore, DA Lockner. Permeability reduction in granite under hydrothermal conditions. Journal of Geophysical Research: Solid Earth. 106 (2001) 30551-60, doi: 10.1029/2000jb000010.

[8] Aben FM, M-L Doan, J-P Gratier, F Renard. Experimental postseismic recovery of fractured rocks assisted by calcite sealing. Geophys Res Lett. 44 (2017) 7228-38, doi: http://dx.doi.org/10.1002/2017GL073965.

[9] Elkhoury JE, RL Detwiler, P Ameli. Can a fractured caprock self-heal? 417 (2015) 99-106, doi: http://dx.doi.org/10.1016/j.epsl.2015.02.010.

[10] Griffiths L, MJ Heap, F Wang, D Daval, HA Gilg, P Baud, et al. Geothermal implications for fracture-filling hydrothermal precipitation. Geothermics. 64 (2016) 235-45, doi: http://dx.doi.org/10.1016/j.geothermics.2016.06.006.

961 [11] Menefee AH, NJ Welch, LP Frash, W Hicks, JW Carey, BR Ellis. Rapid Mineral Precipitation
962 During Shear Fracturing of Carbonate-Rich Shales. Journal of Geophysical Research: Solid Earth. 125
963 (2020) e2019JB018864, doi: 10.1029/2019jb018864.

964 [12] Berkowitz B. Characterizing flow and transport in fractured geological media: A review. Adv Water
965 Resour. 25 (2002) 861-84.

966 [13] Deng H, N Spycher. Modeling Reactive Transport Processes in Fractures. Reviews in Mineralogy
967 and Geochemistry. 85 (2019) 49, doi: 10.2138/rmg.2019.85.3.

968 [14] Brunet JPL, L Li, ZT Karpyn, NJ Huerta. Fracture opening or self-sealing: Critical residence time as
969 a unifying parameter for cement-CO2-brine interactions. International Journal of Greenhouse Gas Control.
970 47 (2018) 25-37, doi: 10.1016/j.ijggc.2016.01.024.

971 [15] Huerta NJ, MA Hesse, SL Bryant, BR Strazisar, CL Lopano. Experimental Evidence for Self-
972 Limiting Reactive Flow through a Fractured Cement Core: Implications for Time-Dependent Wellbore
973 Leakage. Environ Sci Technol. 47 (2013) 269-75, doi: 10.1021/es3013003.

974 [16] Cao P, ZT Karpyn, L Li. Self-healing of cement fractures under dynamic flow of CO2-rich brine.
975 Water Resour Res. 51 (2015), doi: 10.1002/2014wr016162.

976 [17] Garcia-Rios M, L Luquot, JM Soler, J Cama. Influence of the flow rate on dissolution and
977 precipitation features during percolation of CO2-rich sulfate solutions through fractured limestone
978 samples. Chem Geol. 414 (2016) 95-108, doi: http://dx.doi.org/10.1016/j.chemgeo.2015.09.005.

979 [18] Kim S, JC Santamarina. Geometry-coupled reactive fluid transport at the fracture scale: application to
980 CO2 geologic storage. Geofluids. 16 (2016) 329-41, doi: 10.1111/gfl.12152.

981 [19] Cuthbert MO, LA McMillan, S Handley-Sidhu, MS Riley, DJ Tobler, VR Phoenix. A Field and
982 Modeling Study of Fractured Rock Permeability Reduction Using Microbially Induced Calcite
983 Precipitation. Environ Sci Technol. 47 (2013) 13637-43, doi: 10.1021/es402601g.

984 [20] Mountassir GE, RJ Lunn, H Moir, E MacLachlan. Hydrodynamic coupling in microbially mediated
985 fracture mineralization: Formation of self-organized groundwater flow channels. Water Resour Res. 50
986 (2013) 1-16, doi: 10.1002/2013wr013578.

987 [21] Phillips AJ, AB Cunningham, R Gerlach, R Hiebert, C Hwang, BP Lomans, et al. Fracture Sealing
988 with Microbially-Induced Calcium Carbonate Precipitation: A Field Study. Environ Sci Technol. 50
989 (2016) 4111-7, doi: 10.1021/acs.est.5b05559.

990 [22] Wagner R, M Kuhn, V Meyn, H Pape, U Vath, C Clauser. Numerical simulation of pore space
991 clogging in geothermal reservoirs by precipitation of anhydrite. International Journal of Rock Mechanics
992 and Mining Sciences. 42 (2005) 1070-81, doi: 10.1016/j.ijrmms.2005.05.008.

993 [23] Laubach SE, RH Lander, LJ Criscenti, LM Anovitz, JL Urai, RM Pollyea, et al. The Role of
994 Chemistry in Fracture Pattern Development and Opportunities to Advance Interpretations of Geological
995 Materials. Reviews of Geophysics. 57 (2019) 1065– 111, doi: 10.1029/2019rg000671.

996 [24] Ortoleva P, E Merino, C Moore, J Chadam. Geochemical self-organization I. Reaction - transport
997 feedbacks and modeling approach. Am J Sci. 287 (1987) 979-1007.

998 [25] Daccord G, O Lietard, R Lenormand. Chemical dissolution of a porous medium by a reactive fluid: 1.
999 model for the wormholing phenomenon. Chem Eng Sci. 48 (1993) 169-78.

1000 [26] Golfier F, C Zarcone, B Bazin, R Lenormand, D Lasseux, M Quintard. On the ability of a Darcy-
1001 scale model to capture wormhole formation during the dissolution of a porous medium. Journal of Fluid
1002 Mechanics. 457 (2002) 213-54.

1003 [27] Renard F, JP Gratier, P Ortoleva, E Brosse, B Bazin. Self-organization during reactive fluid flow in a
1004 porous medium. Geophys Res Lett. 25 (1998) 385-8.

1005 [28] Hung KM, K Sepehrnoori. A mechanistic model of wormhole growth in carbonate matrix acidizing
1006 and acid fracturing. Journal of Petroleum Technology. 41 (1989) 59-66, doi: 10.2118/16886-PA.

1007 [29] Steefel CI, AC Lasaga. Evolution of dissolution patterns: Permeability change due to coupled flow
1008 and reaction. in: D Melchior, RL Bassett, (Eds.). Chemical Modeling of Aqueous Systems II. American
1009 Chemical Society, Washington DC, 1990. pp. 212-25.

1010 [30] Noiriel C, H Deng. Evolution of planar fractures in limestone: the role of flow rate, mineral
1011 heterogeneity and local transport processes. Chem Geol. 497 (2018) 100-14, doi:
1012 10.1016/j.chemgeo.2018.08.026.

1013 [31] Hoefner ML, HS Fogler. Pore evolution and channel formation during flow and reaction in porous
1014 media. AIChE Journal. 34 (1998) 45-53.

1015 [32] Detwiler RL, RJ Glass, WL Bourcier. Experimental observation of fracture dissolution: The role of
1016 Peclet number on evolving aperture variability. Geophys Res Lett. 30 (2003) 1648,
1017 doi:10.029/2003GL017396.

1018 [33] Roded R, E Aharonov, R Holtzman, P Szymczak. Reactive flow and homogenization in anisotropic
1019 media. Water Resour Res. n/a (2020) e2020WR027518, doi: https://doi.org/10.1029/2020WR027518.

1020 [34] Chaudhuri A, H Rajaram, H Viswanathan. Alteration of fractures by precipitation and dissolution in
1021 gradient reaction environments: Computational results and stochastic analysis. Water Resour Res. 44
1022 (2008), doi: W10410

1023 10.1029/2008wr006982.

1024 [35] Chaudhuri A, H Rajaram, H Viswanathan. Fracture alteration by precipitation resulting from thermal
1025 gradients: Upscaled mean aperture-effective transmissivity relationship. Water Resour Res. 48 (2012),
1026 doi: W01601

1027 10.1029/2011wr010983.

1028 [36] Tartakovsky AM, P Meakin, TD Scheibe, BDCW Wood. A smoothed particle hydrodynamics model
1029 for reactive transport and mineral precipitation in porous and fractured porous media. Water Resour Res.
1030 43 (2007), doi: 10.1029/2005wr004770.

1031 [37] Jones TA, RL Detwiler. Mineral Precipitation in Fractures: Using the Level-Set Method to Quantify
1032 the Role of Mineral Heterogeneity on Transport Properties. Water Resour Res. 55 (2019) 4186-206, doi:
1033 10.1029/2018wr024287.

1034 [38] Yoo S-Y, Y Kuroda, Y Mito, T Matsuoka, M Nakagawa, A Ozawa, et al. A geochemical clogging
1035 model with carbonate precipitation rates under hydrothermal conditions. Appl Geochem. 30 (2013) 67-74,
1036 doi: https://doi.org/10.1016/j.apgeochem.2012.07.018.

1037 [39] Kang Q, D Zhang, S Chen. Simulation of dissolution and precipitation in porous media. Journal of
1038 Geophysical Research: Solid Earth. 108 (2003), doi: 10.1029/2003jb002504.

1039 [40] Sallès J, JF Thovert, PM Adler. Deposition in porous media and clogging. Chem Eng Sci. 48 (1993)
1040 2839-58, doi: https://doi.org/10.1016/0009-2509(93)80031-K.

1041 [41] Liu JS, JC Sheng, A Polak, D Elsworth, H Yasuhara, A Grader. A fully-coupled hydrological-
1042 mechanical-chemical model for fracture sealing and preferential opening. International Journal of Rock
1043 Mechanics and Mining Sciences. 43 (2006) 23-36.

1044 [42] Andreani M, L Luquot, P Gouze, M Godard, E Hoise, B Gibert. Experimental Study of Carbon
1045 Sequestration Reactions Controlled by the Percolation of CO2-Rich Brine through Peridotites. Environ Sci
1046 Technol. 43 (2009) 1226-31, doi: 10.1021/es8018429.

1047 [43] Godinho JRA, KM Gerke, AG Stack, PD Lee. The dynamic nature of crystal growth in pores.
1048 Scientific Reports. 6 (2016), doi: 33086

1049 10.1038/srep33086.

[44] Godinho JRA, PJ Withers. Time-lapse 3D imaging of calcite precipitation in a microporous column. Geochim Cosmochim Acta. 222 (2018) 156-70, doi: https://doi.org/10.1016/j.gca.2017.10.024.

[45] Niu Q, C Zhang. Permeability Prediction in Rocks Experiencing Mineral Precipitation and Dissolution: A Numerical Study. Water Resour Res. 55 (2019) 3107-21, doi: 10.1029/2018wr024174.

[46] Dijk P, B Berkowitz. Precipitation and dissolution of reactive solutes in fractures. Water Resour Res. 34 (1998) 457-70.

[47] Lee YJ, JW Morse, DW Wiltschko. An experimentally verified model for calcite precipitation in veins. Chem Geol. 130 (1996) 203-15.

[48] Tartakovsky AM, P Meakin, TD Scheibe, RME West. Simulations of reactive transport and precipitation with smoothed particle hydrodynamics. Journal of Computational Physics. 222 (2007) 654-72.

[49] Kang Q, D Zhang, PC Lichtner, IN Tsimpanogiannis. Lattice Boltzmann model for crystal growth from supersaturated solution. Geophys Res Lett. 31 (2004), doi: 10.1029/2004gl021107.

[50] Morse JW, FT Mackenzie. Geochemical constraints on CaCO3 transport in subsurface sedimentary environments. Chem Geol. 105 (1993) 181-96, doi: https://doi.org/10.1016/0009-2541(93)90125-3.

[51] Noiriel C, CI Steefel, L Yang, J Ajo-Franklin. Upscaling calcium carbonate precipitation rates from pore to continuum scale. Chem Geol. 318-319 (2012) 60–74.

[52] Teng HH, PM Dove, JJ De Yoreo. Kinetics of calcite growth: Surface processes and relationships to macroscopic rate laws. Geochim Cosmochim Acta. 64 (2000) 2255-66, doi: 10.1016/s0016-7037(00)00341-0.

[53] Noiriel C. Resolving time-dependent evolution of pore scale structure, permeability and reactivity using X-ray microtomography. in: CI Steefel, E Emmanuel, L Anovitz, (Eds.). Pore Scale Geochemical Processes Reviews in Mineralogy & Geochemistry Volume 80. Mineralogical Society of America2015. pp. 247-86.

[54] Emmanuel S, B Berkowitz. Mixing-induced precipitation and porosity evolution in porous media. Adv Water Resour. 28 (2005) 337-44.

[55] Smith MM, Y Sholokhova, Y Hao, SA Carroll. CO_2-induced dissolution of low permeability carbonates. Part I: Characterization and experiments. Adv Water Resour. 62 (2013) 370-87, doi: 10.1016/j.advwatres.2013.09.008.

[56] Yang Y, Y Li, J Yao, S Iglauer, L Luquot, K Zhang, et al. Dynamic Pore-Scale Dissolution by CO2-Saturated Brine in Carbonates: Impact of Homogeneous versus Fractured versus Vuggy Pore Structure. Water Resour Res. n/a (2020) e2019WR026112, doi: 10.1029/2019wr026112.

[57] Yoon H, J Major, T Dewers, P Eichhubl. Application of a pore-scale reactive transport model to a natural analog for reaction-induced pore alterations. Journal of Petroleum Science and Engineering. 155 (2017) 11-20, doi: http://dx.doi.org/10.1016/j.petrol.2017.01.002.

[58] Gale JFW, RH Lander, RM Reed, SE Laubach. Modeling fracture porosity evolution in dolostone. Journal of Structural Geology. 32 (2010) 1201-11, doi: https://doi.org/10.1016/j.jsg.2009.04.018.

[59] Fall A, P Eichhubl, SP Cumella, RJ Bodnar, SE Laubach, SP Becker. Testing the basin-centered gas accumulation model using fluid inclusion observations: southern Piceance Basin, Colorado. . AAPG Bulletin. 96 (2012) 2297-318, doi: https://doi.org/10.1306/05171211149.

[60] Noiriel C, CI Steefel, L Yang, D Bernard. Effects of pore-scale heterogeneous precipitation on permeability and flow Adv Water Resour. 95 (2016) 125-37, doi: http://dx.doi.org/10.1016/j.advwatres.2015.11.013.

[61] Fernandez-Martinez A, Y Hu, B Lee, Y-S Jun, GA Waychunas. In Situ Determination of Interfacial Energies between Heterogeneously Nucleated CaCO3 and Quartz Substrates: Thermodynamics of CO2 Mineral Trapping. Environ Sci Technol. 47 (2013) 102-9, doi: 10.1021/es3014826.

[62] De Yoreo JJ, PG Vekilov. Principles of crystal nucleation and growth. in: PM Dove, JJ DeYoreo, S Weiner, (Eds.). Biomineralization2003. pp. 57-93.

[63] Lioliou MG, CA Paraskeva, PG Koutsoukos, AC Payatakes. Heterogeneous nucleation and growth of calcium carbonate on calcite and quartz. Journal of Colloid and Interface Science. 308 (2007) 421-8, doi: 10.1016/j.jcis.2006.12.045.

[64] Lin YP, PC Singer. Effects of seed material and solution composition on calcite precipitation. Geochim Cosmochim Acta. 69 (2005) 4495-504, doi: 10.1016/j.gca.2005.06.002.

[65] Putnis A, G Mauthe. The effect of pore size on cementation in porous rocks. Geofluids. 1 (2001) 37-41, doi: 10.1046/j.1468-8123.2001.11001.x.

[66] Pape H, C Clauser, J Iffland, R Krug, R Wagner. Anhydrite cementation and compaction in geothermal reservoirs: Interaction of pore-space structure with flow, transport, P-T conditions, and chemical reactions. International Journal of Rock Mechanics and Mining Sciences. 42 (2005) 1056-69, doi: 10.1016/j.ijrmms.2005.05.007.

[67] Nollet S, C Hilgers, JL Urai. Experimental study of polycrystal growth from an advecting supersaturated fluid in a model fracture. Geofluids. 6 (2006) 185-200, doi: 10.1111/j.1468-8123.2006.00142.x.

[68] Manaka M, T Takemura, M Takahashi. Water-Pathway Sealing by Crystallization under Advective Supersaturated Solution Conditions. Materials Transactions. 49 (2008) 2365-70, doi: 10.2320/matertrans.M-MRA2008823.

[69] Bons PD, MA Elburg, E Gomez-Rivas. A review of the formation of tectonic veins and their microstructures. Journal of Structural Geology. 43 (2012) 33-62, doi: https://doi.org/10.1016/j.jsg.2012.07.005.

[70] Hilgers C, JL Urai. Experimental study of syntaxial vein growth during lateral fluid flow in transmitted light: first results. Journal of Structural Geology. 24 (2002) 1029-43, doi: 10.1016/s0191-8141(01)00089-x.

[71] Molins S, P Knaber. Multiscale Approaches in Reactive Transport Modelling. Reviews in Mineralogy and Geochemistry. 85 (2019) 27-48, doi: 10.2138/rmg.2019.85.2.

[72] Seigneur N, E L'Hôpital, A Dauzères, J Sammaljärvi, M Voutilainen, PE Labeau, et al. Transport properties evolution of cement model system under degradation-Incorporation of a pore-scale approach into reactive transport modelling. Physics and Chemistry of the Earth Parts A/B/C. 99 (2017) 95-109 doi: https://doi.org/10.1016/j.pce.2017.05.007.

[73] Yoon H, Q Kang, A Valocchi. Lattice Boltzmann based approaches for reactive transport with pore and flow alteration. in: CI Steefel, S Emmanuel, L Anovitz, (Eds.). Pore Scale Geochemical Processes Reviews in Mineralogy & Geochemistry Volume 802015. pp. this volume.

[74] Ahkami M, A Parmigiani, PR Di Palma, MO Saar, X-Z Kong. A lattice-Boltzmann study of permeability-porosity relationships and mineral precipitation patterns in fractured porous media. Computational Geosciences. (2020), doi: 10.1007/s10596-019-09926-4.

[75] Steefel CI, DJ DePaolo, PC Lichtner. Reactive transport modeling: An essential tool and a new research approach for the Earth sciences. Earth Planet Sci Lett. 240 (2005) 539-58.

[76] Beckingham LE. Evaluation of Macroscopic Porosity-Permeability Relationships in Heterogeneous Mineral Dissolution and Precipitation Scenarios. Water Resour Res. (2017), doi: http://dx.doi.org/10.1002/2017WR021306.

[77] Seigneur N, KU Mayer, CI Steefel. Reactive Transport in Evolving Porous Media. Reviews in Mineralogy and Geochemistry. 85 (2019) 197-238, doi: 10.2138/rmg.2019.85.7.

[78] Poonoosamy J, C Westerwalbesloh, G Deissmann, M Mahrous, E Curti, SV Churakov, et al. A microfluidic experiment and pore scale modelling diagnostics for assessing mineral precipitation and dissolution in confined spaces. Chem Geol. 528 (2019) 119264, doi: https://doi.org/10.1016/j.chemgeo.2019.07.039.

[79] Poonoosamy J, G Kosakowski, LR Van Loon, U Mäder. Dissolution-precipitation processes in tank experiments for testing numerical models for reactive transport calculations: Experiments and modelling. Journal of contaminant hydrology. 177 (2015) 1-17.

[80] Xie M, KU Mayer, F Claret, P Alt-Epping, D Jacques, C Steefel, et al. Implementation and evaluation of permeability-porosity and tortuosity-porosity relationships linked to mineral dissolution-precipitation. Computational geosciences. 19 (2015) 655-71.

[81] Deng H, S Molins, C Steefel, D DePaolo, M Voltolini, L Yang, et al. A 2.5D Reactive Transport Model for Fracture Alteration Simulation. Environ Sci Technol. 50 (2016) 7564-71, doi: 10.1021/acs.est.6b02184.

[82] Noiriel C, P Gouze, B Made. 3D analysis of geometry and flow changes in a limestone fracture during dissolution. Journal of Hydrology. 486 (2013) 211-23, doi: 10.1016/j.jhydrol.2013.01.035.

[83] van der Lee J, L De Windt, V Lagneau, P Goblet. Module-oriented modeling of reactive transport with HYTEC. Computers & Geosciences. 29 (2003) 265-75.

[84] Seigneur N, V Lagneau, J Corvisier, A Dauzères. Recoupling flow and chemistry in variably saturated reactive transport modelling - An algorithm to accurately couple the feedback of chemistry on water consumption, variable porosity and flow. Adv Water Resour. 122 (2018) 355-66, doi: https://doi.org/10.1016/j.advwatres.2018.10.025.

[85] Brush DJ, NR Thomson. Fluid flow in synthetic rough-walled fractures: Navier-Stokes, Stokes, and local cubic law simulations. Water Resour Res. 39 (2003) 5-1-5-15.

[86] Darcy H. Les fontaines publiques de la ville de Dijon. Dalmont, Paris, 1856.

[87] Lasaga AC. Transition State Theory. in: AC Lasaga, and Kirkpatrick, R.J, (Ed.). Kinetics of Geochemical Process. Mineralogical Society of America1981. pp. 135-69.

[88] Li YH, S Gregory. Diffusion of ions in sea water and deep-sea sediments. Geochim Cosmochim Acta. 38 (1974) 703-14.

[89] Carman PC. Fluid flow through granular beds. Transaction for Institute of Chemical Engineer. 15 (1937) 150-66.

1170 [90] Renard P, G de Marsily. Calculating equivalent permeability: a review. Adv Water Resour. 20 (1997)
1171 253-78, doi: https://doi.org/10.1016/S0309-1708(96)00050-4.

1172 [91] Glover PWJ, K Matsuki, R Hikima, K Hayashi. Synthetic rough fractures in rocks. Journal of
1173 Geophysical Research. 103 (1998) 9609-20.

1174 [92] Wu YX, S Hubbard, KH Williams, J Ajo-Franklin. On the complex conductivity signatures of calcite
1175 precipitation. Journal of Geophysical Research-Biogeosciences. 115 (2010) 10, doi: G00g04

1176 10.1029/2009jg001129.

1177 [93] Lee YJ, JW Morse. Calcite precipitation in syntetic veins: implications for the time and fluid volume
1178 necessary for vein filling. Chem Geol. 156 (1999) 151-70.

1179 [94] Noiriel C, P Gouze, B Madé. Time-resolved 3D characterisation of flow and dissolution patterns in a
1180 single rough-walled fracture. in: J Krasny, J Sharp, (Eds.). IAH Selected Papers Series 9 on Groundwater
1181 in Fractured Rocks. Taylor & Francis2007. pp. 629-42.

1182 [95] Morse JW, RS Arvidson. The dissolution kinetics of major sedimentary carbonate minerals. Earth-
1183 Science Reviews. 58 (2002) 51-84.

1184 [96] Noiriel C, B Madé, P Gouze. Impact of coating development on the hydraulic and transport properties
1185 in argillaceous limestone fracture. Water Resour Res. 43 (2007) W09046, doi:10.1029/2006WR005379.

1186 [97] Ellis BR, JP Fitts, GS Bromhal, DL McIntyre, R Tappero, CA Peters. Dissolution-driven
1187 permeability reduction of a fractured carbonate caprock. Environmental Engineering Science. 30 (2013)
1188 187-93, doi: 10.1089/ees.2012.0337.

1189 [98] Stockmann GJ, D Wolff-Boenisch, SR Gislason, EH Oelkers. Do carbonate precipitates affect
1190 dissolution kinetics? 1: Basaltic glass. Chem Geol. 284 (2011) 306-16, doi:
1191 10.1016/j.chemgeo.2011.03.010.

1192 [99] Steefel CI, P Van Cappellen. A new kinetic approach to modeling water-rock interaction - The role of
1193 nulceation, precursors, and Ostwald ripening. Geochim Cosmochim Acta. 54 (1990) 2657-77, doi:
1194 10.1016/0016-7037(90)90003-4.

1195 [100] Kile DE, DD Eberl, AR Hoch, MM Reddy. An assessment of calcite crystal growth mechanisms
1196 based on crystal size distributions. Geochim Cosmochim Acta. 64 (2000) 2937-50, doi:
1197 https://doi.org/10.1016/S0016-7037(00)00394-X.

[101] Ye Z, A Ghassemi, T Kneafsey. Deformation, Failure and Permeability Evolution of Sealed Fractures in EGS Collab Poorman Schist. 45th Workshop on Geothermal Reservoir Engineering, Stanford University, Stanford, California, 2020.

[102] Zheng Q, S Dickson, Y Guo. Influence of aperture field heterogeneity and anisotropy on dispersion regimes and dispersivity in single fractures. Journal of Geophysical Research: Solid Earth. 114 (2009), doi: 10.1029/2007jb005161.

[103] Guren MG, CV Putnis, G Montes-Hernandez, HE King, F Renard. Direct imaging of coupled dissolution-precipitation and growth processes on calcite exposed to chromium-rich fluids. Chem Geol. 552 (2020) 119770, doi: https://doi.org/10.1016/j.chemgeo.2020.119770.

[104] Kumari D QX, Pan X, Achal V, Li Q, Gadd GM. . Microbially-induced Carbonate Precipitation for Immobilization of Toxic Metals. Advances in Applied Microbiology. 94 (2016) 79-108, doi: 10.1016/bs.aambs.2015.12.002.

[105] Li L, CA Peters, MA Celia. Effects of mineral spatial distribution on reaction rates in porous media. Water Resour Res. 43 (2007) doi10.1029/2005WR004848.

[106] Jones TA, RLCGL Detwiler. Fracture sealing by mineral precipitation: The role of small-scale mineral heterogeneity. Geophys Res Lett. 43 (2016) 7564-71, doi: 10.1002/2016gl069598.

[107] Beckingham LE, CI Steefel, AM Swift, M Voltolini, L Yang, LM Anovitz, et al. Evaluation of accessible mineral surface areas for improved prediction of mineral reaction rates in porous media. Geochim Cosmochim Acta. 205 (2017) 31-49, doi: http://doi.org/10.1016/j.gca.2017.02.006.